INPP5E regulates phosphoinositide-dependent cilia transition zone function

Jennifer M. Dyson,[1] Sarah E. Conduit,[1] Sandra J. Feeney,[1] Sandra Hakim,[1] Tia DiTommaso,[2] Alex J. Fulcher,[3] Absorn Sriratana,[1] Georg Ramm,[3] Kristy A. Horan,[1] Rajendra Gurung,[1] Carol Wicking,[5] Ian Smyth,[2,4] and Christina A. Mitchell[1]

[1]Cancer Program, Monash Biomedicine Discovery Institute and Department of Biochemistry and Molecular Biology, [2]Department of Biochemistry and Molecular Biology, [3]Monash Micro Imaging, and [4]Development and Stem Cells Program, Department of Anatomy and Developmental Biology, Monash University, Clayton, Victoria 3800, Australia
[5]Institute for Molecular Bioscience, The University of Queensland, Brisbane, Queensland 4072, Australia

Human ciliopathies, including Joubert syndrome (JBTS), arise from cilia dysfunction. The inositol polyphosphate 5-phosphatase INPP5E localizes to cilia and is mutated in JBTS. Murine *Inpp5e* ablation is embryonically lethal and recapitulates JBTS, including neural tube defects and polydactyly; however, the underlying defects in cilia signaling and the function of INPP5E at cilia are still emerging. We report *Inpp5e*$^{-/-}$ embryos exhibit aberrant Hedgehog-dependent patterning with reduced Hedgehog signaling. Using mouse genetics, we show increasing Hedgehog signaling via Smoothened M2 expression rescues some *Inpp5e*$^{-/-}$ ciliopathy phenotypes and "normalizes" Hedgehog signaling. INPP5E's phosphoinositide substrates PI(4,5)P_2 and PI(3,4,5)P_3 accumulated at the transition zone (TZ) in Hedgehog-stimulated *Inpp5e*$^{-/-}$ cells, which was associated with reduced recruitment of TZ scaffolding proteins and reduced Smoothened levels at cilia. Expression of wild-type, but not 5-phosphatase-dead, INPP5E restored TZ molecular organization and Smoothened accumulation at cilia. Therefore, we identify INPP5E as an essential point of convergence between Hedgehog and phosphoinositide signaling at cilia that maintains TZ function and Hedgehog-dependent embryonic development.

Introduction

Primary cilia coordinate several signaling cascades during embryonic development. Cilia are anchored to the plasma membrane by transition fibers that connect the basal body to the plasma membrane, separating the cilia and cytosolic compartments. The intervening region between the basal body and axoneme is termed the transition zone (TZ) and acts a diffusion barrier to contribute to cilia entry and retention mechanisms (Hu et al., 2010; Chih et al., 2011; Williams et al., 2011; Reiter et al., 2012; Szymanska and Johnson, 2012; Jensen et al., 2015). Human ciliopathy syndromes arise from cilia dysfunction and share common phenotypes, including polycystic kidneys, neural tube defects, and polydactyly (Waters and Beales, 2011; Roberson et al., 2015). Growing evidence suggests TZ dysfunction may underlie ciliopathies (Chih et al., 2011; Huang et al., 2011; Sang et al., 2011; Williams et al., 2011; Szymanska and Johnson, 2012; Roberson et al., 2015; Lambacher et al., 2016), although the molecular composition and mechanisms governing TZ function are little characterized.

Vertebrate Hedgehog (Hh) signaling is essential for tissue patterning and embryonic development. Upon Sonic Hedgehog (Shh) ligand binding to Patched (Ptch1), signal transduction is critically dependent on the ciliary accumulation and retention of the transmembrane receptor smoothened (SMO), which in turn modulates Hh-target gene transcription via glioma-associated oncogene hologue-1 (GLI) transcription factors (Corbit et al., 2005; Haycraft et al., 2005; Rohatgi et al., 2007, 2009; Milenkovic et al., 2009; Goetz and Anderson, 2010; Waters and Beales, 2011). However, the mechanisms that govern SMO cilia entry and exit are still emerging. GLI2 and GLI3 predominantly regulate Hh-dependent transcription during development; GLI2 acts primarily as an activator (GLI2A), whereas GLI3 mainly represses transcription after its proteolytic processing to a truncated repressor form (GLI3R; Haycraft et al., 2005; Hui and Angers, 2011). The G protein–coupled receptor GPR161 is a negative regulator of Hh signaling that is recruited to cilia via TULP3 (Tubby-like protein 3) and the IFT-A (intraflagellar transport) complex and promotes GLI3R production (Mukhopadhyay et al., 2013). Recent studies show GPR161 is removed

Correspondence to Christina A. Mitchell: christina.mitchell@monash.edu

Abbreviations used: DSHB, Developmental Studies Hybridoma Bank; E, embryonic day; Hh, Hedgehog; JBTS, Joubert syndrome; MEF, mouse embryonic fibroblast; MFI, mean fluorescence intensity; PI, phosphoinositide; PI3K, phosphoinositide 3-kinase; pMEF, primary MEF; Ptch, Patched; ROI, region of interest; RPE, retinal pigment epithelial; SAG, smoothened agonist; Shh, Sonic Hedgehog; SMO, Smoothened; TZ, transition zone.

The Rockefeller University Press $30.00
J. Cell Biol. Vol. 216 No. 1 247–263
https://doi.org/10.1083/jcb.201511055

from cilia via the accumulation of active SMO at cilia after the induction of Hh signaling (Pal et al., 2016). Consequently, *Smo* deletion is associated with increased GPR161 levels at cilia (Pal et al., 2016).

Phosphoinositides (PIs) play major roles in regulating many cellular functions, including vesicular trafficking (Balla, 2013). Recent studies have localized some, but not all, PI species to primary cilia (Vieira et al., 2006; Wei et al., 2008; Franco et al., 2014; Chávez et al., 2015; Garcia-Gonzalo et al., 2015; Jensen et al., 2015; Park et al., 2015); however, their functional role and turnover in response to cilia signaling has not been reported. The inositol polyphosphate 5-phosphatase INPP5E is mutated in the ciliopathies Joubert syndrome (JBTS) and the rarer mental retardation, truncal obesity, retinal dystrophy and micropenis syndrome (Bielas et al., 2009; Jacoby et al., 2009). Ubiquitous deletion of *Inpp5e* (*Inpp5e*$^{\Delta/\Delta}$) in mice results in embryonic lethality with a phenotype that recapitulates JBTS, including neural tube defects, polydactyly, and polycystic kidneys (Jacoby et al., 2009). INPP5E degrades phosphatidylinositol(4,5)-bisphosphate ($PI(4,5)P_2$) and phosphoinositide 3-kinase (PI3K)–dependent phosphatidylinositol(3,4,5)-trisphosphate ($PI(3,4,5)P_3$), to form PI(4)P and $PI(3,4)P_2$, respectively (Kisseleva et al., 2000; Kong et al., 2000). $PI(4,5)P_2$ signals accumulate at cilia of *Inpp5e* null cells. Hh signaling activates PI3K signaling (Riobó et al., 2006); however, no studies to date have identified $PI(3,4,5)P_3$ signals at cilia or examined whether Hh signaling stimulates the turnover of $PI(4,5)P_2$ and/or $PI(3,4,5)P_3$ at cilia.

Many *INPP5E* missense mutations have been identified in JBTS, and all analyzed to date show reduced 5-phosphatase activity toward $PI(3,4,5)P_3$ and $PI(4,5)P_2$, suggesting increased $PI(4,5)P_2$ and/or $PI(3,4,5)P_3$ may contribute to abnormal development (Bielas et al., 2009; Travaglini et al., 2013). Importantly, INPP5E localization to cilia is dependent on a growing number of JBTS proteins, such as MKS1, that when mutated or deleted result in the loss of INPP5E cilia localization (Humbert et al., 2012; Thomas et al., 2014; Roberson et al., 2015; Slaats et al., 2016). Thus, cilia mislocalization of INPP5E, and thereby loss of INPP5E function at cilia, is suggested as an important mechanism underlying JBTS. Recent studies demonstrate INPP5E may regulate Hh signaling via modulating the $PI(4,5)P_2$-dependent recruitment of GPR161 to cilia (Chávez et al., 2015; Garcia-Gonzalo et al., 2015). However, INPP5E also degrades $PI(3,4,5)P_3$ and regulates PI3K-dependent cilia stability. INPP5E-mediated degradation of PI3K-generated $PI(3,4,5)P_3$ is essential to cilia function (Kisseleva et al., 2002; Jacoby et al., 2009) by yet-to-be-identified mechanisms. In addition, recent studies have shown increased PI3K–AKT–mTOR signaling drives polycystic kidney disease in kidney-tubule–specific *Inpp5e* knockout mice (Hakim et al., 2016).

Here, we show *Inpp5e*$^{-/-}$ mice exhibit abnormal Hh-dependent patterning in vivo and reduced cilia accumulation of the Hh signaling components SMO and GLI2, leading to decreased Hh signaling. Proof-of-principle mouse genetic studies demonstrate *Inpp5e* null ciliopathy phenotypes are in part rescued by constitutive hyperactivation of Hh signaling via SMOM2 expression. At the TZ, $PI(3,4,5)P_3$ signals increase in response to Hh signaling and further increase with *Inpp5e* deletion, leading to changes in the molecular organization and function of the TZ and reduced accumulation of SMO at cilia. Therefore, our study identifies INPP5E as a novel regulator of TZ function that integrates PI3K and Hh signaling at cilia.

Results

Murine deletion of *Inpp5e* results in disordered Hh-dependent patterning and decreased high-level Hh signaling during embryonic development

Recently, INPP5E has been shown to modulate the trafficking of the Hh pathway suppressor GPR161 to cilia and regulate Hh signaling in cultured cells (Chávez et al., 2015; Garcia-Gonzalo et al., 2015). To investigate whether in vivo Hh signaling/patterning is perturbed with *Inpp5e* ablation, we deleted the 5-phosphatase by mating a conditionally modified mouse (floxing exons 2 to 6, *Inpp5e*^{tm1Cmit}; Fig. S1 a), with a germline Cre-deleter strain (*CMV-Cre*), followed by heterozygous matings (*Inpp5e*$^{tm1.1Cmit}$ hereafter *Inpp5e*$^{-/-}$). *Inpp5e* deletion in primary mouse embryonic fibroblasts (pMEFs) was confirmed by quantitative RT-PCR (Fig. S1 b). *Inpp5e*$^{-/-}$ embryos died at ∼E18.5, when polycystic kidneys (100%, n = 26/26) were observed (Fig. S1 c). From midgestation, *Inpp5e*$^{-/-}$ embryos showed multiple abnormalities consistent with cilia dysfunction and/or aberrant Hh signaling, including bilateral anophthalmos (100%, n = 26/26) in the presence or absence of exencephaly (65%, n = 17/26; Fig. 1, a and b), cleft palate (76%, n = 20/26; Figs. 1 c and S1 d), and single-digit preaxial hindlimb polydactyly (100%, n = 26/26; Fig. 1 d). These defects are consistent with a previous study of *Inpp5e*$^{\Delta/\Delta}$ embryos, but in addition, we identify edema (69%, n = 18/26; Fig. 1, a and b, arrows), delayed and reduced vertebral body ossification (100%, n = 4/4; Figs. 1 e and S1 e), reduced and absent ossification of the occipital bone (50%, n = 2/4; Fig. S1 f) and 13th rib (75%, n = 3/4; Figs. 1 f and S1 g), respectively, and pulmonary hypoplasia coupled with left lung isomerization (100%, n = 6/6; Fig. 1 g). This phenotypic spectrum broadly phenocopies *INPP5E* mutations in JBTS (Bielas et al., 2009; Jacoby et al., 2009).

To assess the contribution of INPP5E to Hh signaling in vivo, we examined the patterning of neuroprogenitor cells in the developing neural tube of *Inpp5e*$^{-/-}$ embryos which is highly dependent on the fine balance of GLI activator and repressor function. *Shh* secreted from the notochord induces the floor plate and specifies motor neurons and various classes of interneurons across the dorsoventral axis in a concentration-dependent manner. Induction of the ventral floor plate requires the highest level of Hh signaling and is primarily dependent on GLI2 activator (GLI2A) function, whereas GLI3R in the dorsal neural tube defines the dorsal extent of intermediate neuroprogenitors (Ding et al., 1998; Matise et al., 1998; Litingtung and Chiang, 2000). At embryonic day 10.5 (E10.5), *Shh* expression was abrogated (Fig. 1 h) and cell morphology was altered (Fig. 1 j, arrowheads) in the *Inpp5e*$^{-/-}$ floor-plate region, suggesting cells requiring the highest levels of Shh were incorrectly specified. Islet1-positive motor neuron progenitors were detected ectopically in the midline and expanded dorsally in *Inpp5e*$^{-/-}$ embryos (Fig. 1, i and j). Nkx2.2-positive P3 interneuron progenitors were mislocalized in the ventral midline (Fig. 1 k), and Pax6-positive P2 interneuron progenitors shifted dorsally in *Inpp5e*$^{-/-}$ embryos (Fig. 1 l). Quantification revealed an increased area and dorsal expansion of Pax6-positive progenitors in the *Inpp5e*$^{-/-}$ neural tube but no change in ventral positioning (Fig. 1 m). Interestingly, the neural tube patterning in *Inpp5e*$^{-/-}$ embryos is similar to mice with mutations in *Arl13b*, which is also mutated in JBTS, and ARL13B is required for INPP5E cilia localization (Caspary et al., 2007; Humbert et al., 2012). In both *Arl13b* and *Inpp5e*$^{-/-}$

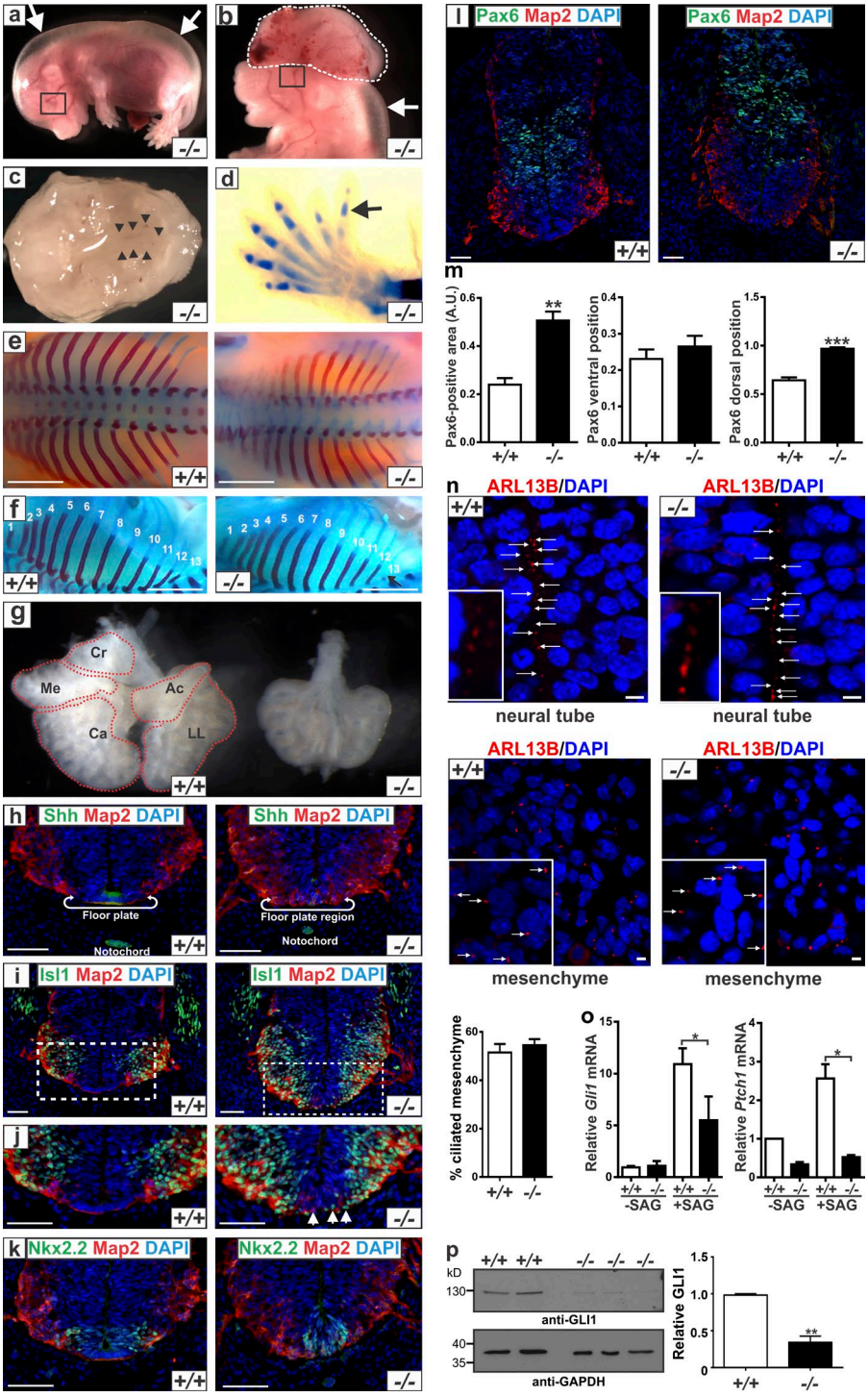

Figure 1. **Germline deletion of *Inpp5e* leads to developmental abnormalities, abnormal Hh-dependent patterning, reduced Hh signaling, and normal cilia number.** (a–c) E15.5 *Inpp5e*$^{-/-}$ (−/−) embryo. (a) Boxed region indicates absence of eye. (b) Dotted line indicates exencephaly. (a and b) Arrow indicates edema. (c) Arrowheads indicate the edges of the unfused palatal shelves. (d) Alcian blue (cartilage) and alizarin red (bone) staining of E15.5 *Inpp5e*$^{-/-}$ (−/−) hindlimb. Arrow indicates extra digit. (e–f) Alcian blue (cartilage) and alizarin red (bone) staining of E16.5 *Inpp5e*$^{+/+}$ (+/+) and *Inpp5e*$^{-/-}$ (−/−) embryos. (e and f) View of vertebral column (e) and ribs (f) numbered 1–13. Bars, 1.5 mm. (g) *Inpp5e*$^{+/+}$ (+/+) and *Inpp5e*$^{-/-}$ (−/−) E12.5 lung. Red dotted outline indicates cranial lobe (Cr), medial lobe (Me), caudal lobe (Ca), accessory lobe (Ac), and left lung (LL). (h–l) *Inpp5e*$^{+/+}$ (+/+) and *Inpp5e*$^{-/-}$ (−/−) E10.5 ventral neural tube transverse sections costained with DAPI (blue) and Map2 (red) antibodies and Shh (h), Isl1 (i and j), Nkx2.2 (k), or Pax6 (l) antibodies (green). Zoom of boxed region in panel i is shown in panel j. Arrowhead indicates abnormal cell morphology. *n* = 3 mice per genotype. Bars, 50 µm. (m) *Inpp5e*$^{+/+}$ (+/+) and *Inpp5e*$^{-/-}$ (−/−) E10.5 ventral neural tube transverse sections costained with DAPI, Map2, and Pax6 antibodies as shown in panel l were scored for the Pax6-positive area (left), the Pax6 ventral boundary (middle), and the Pax6 dorsal boundary (right). Bars represent mean ± SEM. *n* = 3 mice per genotype; **, P < 0.01; ***, P < 0.001. A.U., arbitrary units. (n) *Inpp5e*$^{+/+}$ (+/+) and *Inpp5e*$^{-/-}$ (−/−) E10.5 embryo transverse sections costained with DAPI and ARL13B antibodies. Top panels show the neural tube, and lower panels show the perineural mesenchyme. Bars, 10 µm. (n, bottom graph) The percentage of ARL13B-positive ciliated cells in the perineural mesenchyme was scored (% ciliated mesenchyme). Bars represent mean ± SEM. *n* = 3 mice/genotype. (o) RNA extracted from untreated and SAG-treated *Inpp5e*$^{+/+}$ (+/+) and *Inpp5e*$^{-/-}$ (−/−) pMEFs was subjected to quantitative RT-PCR and normalized to *Actb* or *Gapdh*. The relative transcript level of *Gli1* (left) and *Ptch1* (right) was determined and normalized to 1 in *Inpp5e*$^{+/+}$ (+/+). Bars represent mean ± SEM. *n* = 3 pMEF lines per genotype; *, P < 0.05. (p) SAG-treated *Inpp5e*$^{+/+}$ (+/+) and *Inpp5e*$^{-/-}$ (−/−) pMEF lysates were immunoblotted with GLI1 antibodies (top) and reprobed with GAPDH antibodies (bottom). The relative expression of GLI1 was determined by densitometry using GAPDH as a loading control and normalized to 1 in *Inpp5e*$^{+/+}$ (+/+). In the graph, bars represent mean ± SEM. *n* = 3 pMEF lines per genotype; **, P < 0.01.

mutant mice, floor plate cells that require the highest level of Hh signaling are not specified, and cells dependent on intermediate Hh levels are expanded. Defects in GLI activator are proposed to underlie the abnormal neural tube patterning in *Arl13b* mutant mice, whereas GLI3 repressor was unaffected (Caspary et al., 2007). The similarities between the *Arl13b* and *Inpp5e* mutants suggests defective GLI activator may also contribute to the disordered neural tube patterning with *Inpp5e* deletion. However, *Inpp5e* ablation has recently been shown to promote GPR161 cilia accumulation. GPR161 negatively regulates Hh signaling via increasing cyclic AMP levels and thereby promoting GLI3 repressor formation (Mukhopadhyay et al., 2013; Chávez et al., 2015; Garcia-Gonzalo et al., 2015). Indeed, GPR161 is highly expressed in the developing neural tube, and its deletion in mice gives rise to a ventralized neural tube phenotype similar to IFT-A mutants (Matteson et al., 2008; Mukhopadhyay et al., 2013). Thus, although the comparative phenotype analysis suggests defective GLI activator contributes to the *Inpp5e*$^{-/-}$ neural tube phenotype, we cannot exclude a role for GLI3 repressor as predicted by the recently described INPP5E–GPR161–GLI3

repressor axis. Overall, our data suggest aberrant Hh signaling may underlie some, but not all, *Inpp5e*$^{-/-}$ phenotypes.

A previous study reports *Inpp5e*$^{\Delta/\Delta}$ cystic renal tubules show reduced cilia number with abnormal morphology (Jacoby et al., 2009); however, these changes were not detected before renal cyst development, suggesting loss of cilia may be a consequence of cytogenesis. Supporting this, we and others have reported *Inpp5e* knockout mouse embryonic fibroblasts (MEFs) show no change in the proportion of ciliated cells (Jacoby et al., 2009; Plotnikova et al., 2015). Using the cilia axoneme marker ARL13B, we surveyed cilia in the *Inpp5e*$^{-/-}$ developing neural tube, revealing no overt changes compared with wild-type embryos (Fig. 1 n, top). Because scoring cilia is difficult in the neural tube, we assessed the surrounding mesenchymal cells (Fig. 1 n, bottom) but found no differences in cilia number or morphology between genotypes (Fig. 1 n, bottom graph). Expression of the Hh-target genes *Gli1* and *Ptch1* and analysis of GLI1 protein levels after the activation of Hh signaling using Smoothened agonist (SAG) are metrics for Hh pathway activation (Chen et al., 2002). pMEFs were isolated from *Inpp5e*$^{+/+}$ and *Inpp5e*$^{-/-}$ embryos. Expression of both *Gli1* and *Ptch1* mRNA (Fig. 1 o) and GLI1 protein (Fig. 1 p) was significantly reduced in SAG stimulated *Inpp5e*$^{-/-}$ pMEFs when compared with *Inpp5e*$^{+/+}$ pMEFs, consistent with attenuation of Hh signaling. Therefore, *Inpp5e*$^{-/-}$ embryos and pMEFs show evidence of reduced Hh signaling and normal cilia number, suggesting the coordination of Hh signaling at cilia may be disrupted with *Inpp5e* deletion.

Enhanced Hh signaling via SMO activation rescues *Inpp5e*$^{-/-}$ mouse phenotypes

The contribution of decreased Hh signaling to the *Inpp5e* null phenotype was assessed using a murine genetics approach. SMOM2 (Trp535Leu) is a constitutively active SMO mutant originally identified in basal cell carcinoma that localizes to cilia independent of the Shh ligand (Xie et al., 1998; Jung et al., 2016). Expression of SMOM2 in mice or in cultured cells results in the hyperactivation of Hh signaling (Corbit et al., 2005; Mao et al., 2006; Wong et al., 2009). Therefore, we reasoned that SMOM2 expression in the context of *Inpp5e* deletion may in part normalize Hh signaling. To this end, *Inpp5e* null mice expressing constitutively active SMO (SMOM2) were generated (*Inpp5e*$^{-/-}$*;CMVCre;SmoM2*). Analysis of E15.5 *Inpp5e*$^{-/-}$*;CMVCre;SmoM2* embryos revealed a striking "rescue" of phenotypes commonly observed in *Inpp5e* null (*Inpp5e*$^{-/-}$;*CMVCre*) single-mutant mice, including complete rescue of the bilateral anophthalmia and exencephaly (Table S1 and Fig. 2, a and b) and partial rescue of the edema (Table S1 and Fig. 2 b), hindlimb polydactyly (Table S1 and Fig. 2 c), and cleft palate (Table S1). In contrast to both the *Inpp5e*$^{-/-}$*;CMV-Cre* and *Inpp5e*$^{+/+}$*;CMVCre;SmoM2* single-mutant mice that show bilateral anophthalmia, formation of the lens, retina, and optic nerve appeared relatively normal in *Inpp5e*$^{-/-}$*;CMVCre;SmoM2* embryos (Fig. 2 e), although one embryo (of eight analyzed) exhibited coloboma (Fig. S2 a). Significantly, at E15.5, the previously unreported complex dysmorphology associated with constitutive SMOM2 signaling during embryonic development (*Inpp5e*$^{+/+}$*;CMVCre;SmoM2*), including the midline expansion (Fig. 2 a, double arrow), fore- and hindlimb polysyndactyly (Table S1 and Fig. 2, c and d), bilateral anophthalmia (Table S1 and Fig. 2, a and e), and loss of neural tube architecture (Table S1 and Fig. S2, b and c), was also rescued by *Inpp5e* ablation. In this context, *Inpp5e*$^{-/-}$*;CMVCre;SmoM2* embryos appeared more like wild-type embryos than either single mutant (Table S1; Fig. 2, a–e; and Fig. S2, b and c). Additionally, despite the same expected frequency, more *Inpp5e*$^{-/-}$*;CMVCre;SmoM2* embryos were harvested and viable at E15.5 relative to *Inpp5e*$^{+/+}$*;CMVCre;SmoM2*, suggesting *Inpp5e* deletion in the context of SMOM2 expression may improve viability. A χ^2 test revealed the observed frequency of genotypes was significantly different from Mendelian ratios ($P = 0.0283$). Next, we examined whether the phenotypic rescue of *Inpp5e*$^{-/-}$*;CMVCre;SmoM2* embryos was associated with the normalization of Hh signaling by measuring *Ptch1* mRNA levels in whole embryos (Fig. 2 f). Importantly, levels of *Ptch1* were comparable in "rescue" *Inpp5e*$^{-/-}$*;CMVCre;SmoM2* embryos and wild-type *Inpp5e*$^{+/+}$*;CMVCre* embryos, and in control studies, *Ptch1* levels were increased in *Inpp5e*$^{+/+}$*;CMVCre;SmoM2* embryos, consistent with SMOM2-induced hyperactivation of Hh signaling (Fig. 2 f). These results reveal expression of SMOM2 recalibrates Hh signaling in the presence of concomitant *Inpp5e* deletion and partially restores some embryonic development defects associated with *Inpp5e* deletion.

Inpp5e deletion reduces Hh-stimulated cilia accumulation of SMO and GLI2

The cilia accumulation and subsequent activation of SMO after Hh stimulation is critical for activating downstream signaling (Corbit et al., 2005). We investigated the cilia localization of Hh pathway components in pMEFs before and after Hh pathway stimulation using SAG, conditions under which SMO accumulates at cilia (Chen et al., 2002; Rohatgi et al., 2007; Wang et al., 2009; Wu et al., 2012). Endogenous SMO was virtually undetected at cilia in nonstimulated *Inpp5e*$^{+/+}$ and *Inpp5e*$^{-/-}$ pMEFs (unpublished data), consistent with other studies (Rohatgi et al., 2007; Wang et al., 2009). In SAG-treated *Inpp5e*$^{+/+}$ pMEFs, endogenous SMO colocalized with acetylated α-tubulin (ac-tubulin) along the cilia axoneme (Fig. 3 a), however, in *Inpp5e*$^{-/-}$ pMEFs, SMO cilia staining was reduced (Fig. 3 a). We measured the mean fluorescence intensity (MFI) of SMO along the axoneme as well as the SMO/ac-tubulin ratio at cilia in both genotypes, which confirmed *Inpp5e* deletion significantly reduced SMO accumulation at cilia after Hh pathway activation (Fig. 3 a).

To determine whether the reduced cilia accumulation of SMO in *Inpp5e*$^{-/-}$ pMEFs is dependent on INPP5E 5-phosphatase degradation of the lipid signals $PI(3,4,5)P_3$ and $PI(4,5)P_2$, wild-type (5-phosphatase-active) HA-INPP5E or 5-phosphatase-dead HA-INPP5E^{D480N} (HA-D480N; Kong et al., 2000) or HA vector controls were expressed at comparable levels in *Inpp5e* null pMEFs (Fig. S3 a) and SMO cilia localization examined (Fig. 3 b, HA vector not depicted; Kong et al., 2006). *Inpp5e*$^{-/-}$ pMEFs were scored positive for rescue of SMO cilia localization when the MFI of SMO at cilia in transfected cells reached 70% or more of wild-type levels. Importantly only ∼15% of *Inpp5e*$^{-/-}$ pMEFs expressing HA-INPP5E^{D480N} qualified for rescue of SMO cilia localization in contrast to ∼75% of cells expressing HA-INPP5E, revealing INPP5E 5-phosphatase activity that degrades $PI(4,5)P_2$ and $PI(3,4,5)P_3$ is essential for the cilia accumulation of SMO (Fig. 3 b). In control studies, HA-INPP5E and HA-INPP5E^{D480N} efficiently localized along the cilia axoneme in *Inpp5e*$^{-/-}$ pMEFs (Fig. S3 b). Therefore expression of wild-type HA-INPP5E, but not HA-INPP5E^{D480N} or vector controls, restored the axoneme localization of SMO in

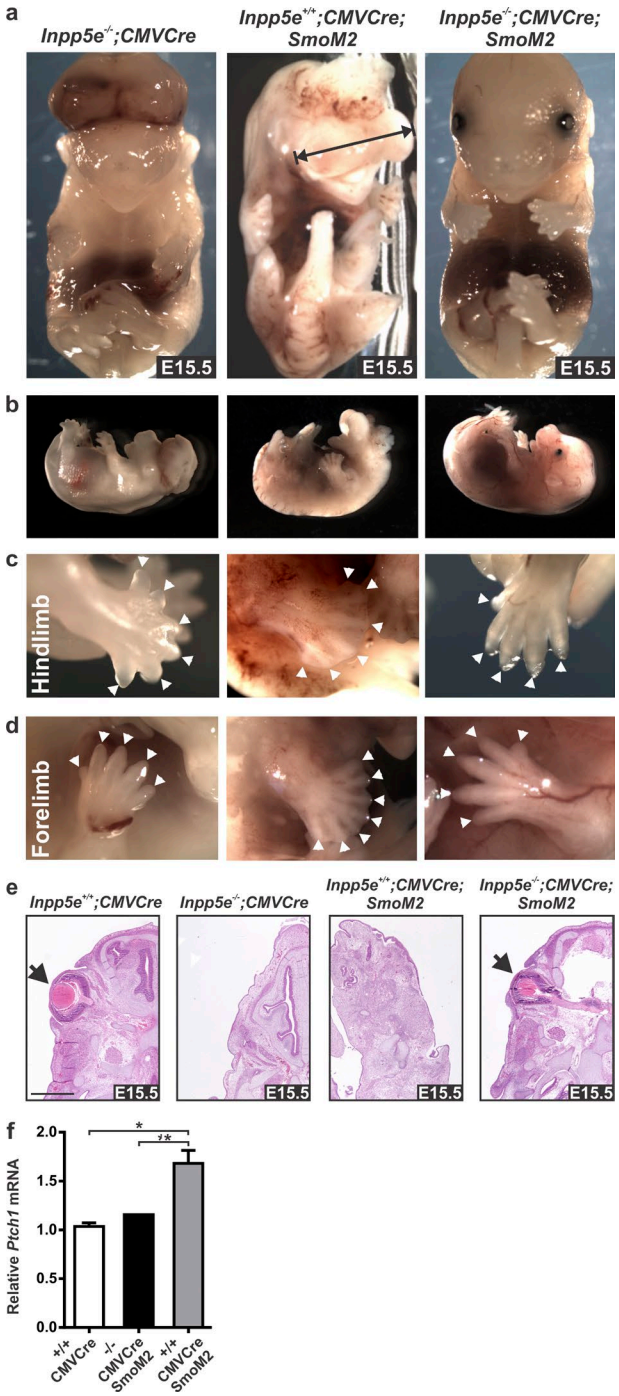

Figure 2. **Expression of SMOM2 rescues *Inpp5e* null phenotypes in vivo.** (a–d) E15.5 *Inpp5e*$^{-/-}$*;CMVCre*, *Inpp5e*$^{+/+}$*;CMVCre;SmoM2* and *Inpp5e*$^{-/-}$*;CMVCre;SmoM2* embryos (a and b), hindlimb (c), and forelimb (d). (a) Double arrow indicates midline expansion. (c and d) Arrowhead indicates digit. (e) E15.5 *Inpp5e*$^{+/+}$*;CMVCre*, *Inpp5e*$^{-/-}$*;CMVCre*, *Inpp5e*$^{+/+}$*;CMVCre;SmoM2*, and *Inpp5e*$^{-/-}$*;CMVCre;SmoM2* embryos. (e) Arrow indicates eye. Bar, 500 µm. (f) RNA extracted from E10.5 *Inpp5e*$^{+/+}$*;CMVCre* (*+/+;CMVCre*), *Inpp5e*$^{-/-}$*;CMVCre;SmoM2* (*-/-;CMVCre;SmoM2*), and *Inpp5e*$^{+/+}$*;CMVCre;SmoM2* (*+/+;CMVCre;SmoM2*) embryos was subjected to quantitative RT-PCR and normalized to *Gapdh*. The relative *Ptch1* transcript level was determined and normalized to 1 in *+/+;CMVCre*. Bars represent mean ± SEM. n = 2 embryos per genotype; *, $P < 0.05$.

Inpp5e$^{-/-}$ pMEFs after Hh pathway activation (Fig. 3 b). Consistent with these observations, *Inpp5e*$^{-/-}$ pMEFs expressing HA-INPP5E, but not vector controls, showed increased *Ptch1* mRNA expression after SAG treatment (Fig. 3 b). Our results contrast those of a recent study that used a SV40-transformed immortalized *Inpp5e*$^{\Delta/\Delta}$ MEF line isolated from E19.5 embryo tail and a commercial SMO antibody and reported no change in SMO cilia levels compared with heterozygous *Inpp5e*$^{+/-}$ MEFs after SAG treatment (Garcia-Gonzalo et al., 2015). Notably, SV40 activates Hh and other signaling pathways and also up-regulates the expression of Hh pathway components, including SMO (Ali-Seyed et al., 2006). SV40-transformed cells are dependent on active Hh signaling for survival (Ali-Seyed et al., 2006). Here, we used multiple low-passage (fewer than five) primary *Inpp5e*$^{-/-}$ MEF lines derived from eviscerated E12.5 embryos and a well-characterized SMO antibody (Milenkovic et al., 2009; Rohatgi et al., 2009; Dorn et al., 2012). These distinct experimental approaches may underlie the apparent discrepancy between these results.

In the absence of Hh activation, GLI2 localizes at the cilia tip at low levels. SAG stimulation promotes GLI2 trafficking and its increased accumulation at the cilia tip, which is causally linked to the cilia enrichment of SMO (Chen et al., 2009; Kim et al., 2009). GLI2 was detected at low levels at cilia in untreated *Inpp5e*$^{+/+}$ and *Inpp5e*$^{-/-}$ pMEFs (unpublished data). After SAG treatment, GLI2 accumulated at the cilia tip immediately distal the axoneme in *Inpp5e*$^{+/+}$ pMEFs (Fig. 3 c); however, in *Inpp5e*$^{-/-}$ pMEFs, GLI2 was more evenly distributed along the axoneme and showed reduced accumulation at the cilia tip in response to SAG (Fig. 3 c), an observation confirmed by cilia tip GLI2 MFI analysis (Fig. 3 c). Together, these findings reveal the cilia accumulation and cilia tip localization of the Hh signal transducers SMO and GLI2, respectively, are reduced in response to Hh pathway activation with *Inpp5e* deletion.

SMO regulates GPR161 levels at cilia by promoting its removal from cilia after Hh pathway activation (Pal et al., 2016). Endogenous GPR161 cilia levels were increased in untreated and SAG-treated *Inpp5e*$^{-/-}$ pMEFs compared with wild-type as described (Fig. 3 d; Garcia-Gonzalo et al., 2015). The reduced accumulation of SMO at cilia in *Inpp5e*$^{-/-}$ pMEFs after Hh pathway activation may contribute to the increased level of GPR161. In addition, GPR161 cilia levels were increased in untreated rescue *Inpp5e*$^{-/-}$*;CMVCre;SmoM2* pMEFs compared with wild-type (Fig. 3 d). These studies show that despite the rescue of some *Inpp5e*$^{-/-}$ phenotypes by concomitant SMOM2 expression, GPR161 is abnormally retained at cilia. Therefore, the regulation of GPR161 by INPP5E is not the only mechanism by which the 5-phosphatase regulates Hh signaling, and the partial rescue of *Inpp5e*$^{-/-}$*;CMVCre;SmoM2* is not caused by the relocalization of GPR161 away from cilia.

To evaluate INPP5E function in regulating cilia membrane composition the localization of cilia-localized receptors not involved in or spatially regulated by Hh signaling was investigated. Endogenous polycystin II (Fig. 3 e) and recombinant FLAG-tagged HTR6 (Fig. S3 c) localized to cilia in untreated *Inpp5e*$^{+/+}$ and *Inpp5e*$^{-/-}$ pMEFs. However, after SAG treatment, both receptors showed reduced cilia localization in *Inpp5e*$^{-/-}$ pMEFs compared with wild-type cells (Figs. 3 e and S3 c), also shown by polycystin II cilia MFI analysis (Fig. 3 e). These findings are consistent with the reported mislocalization

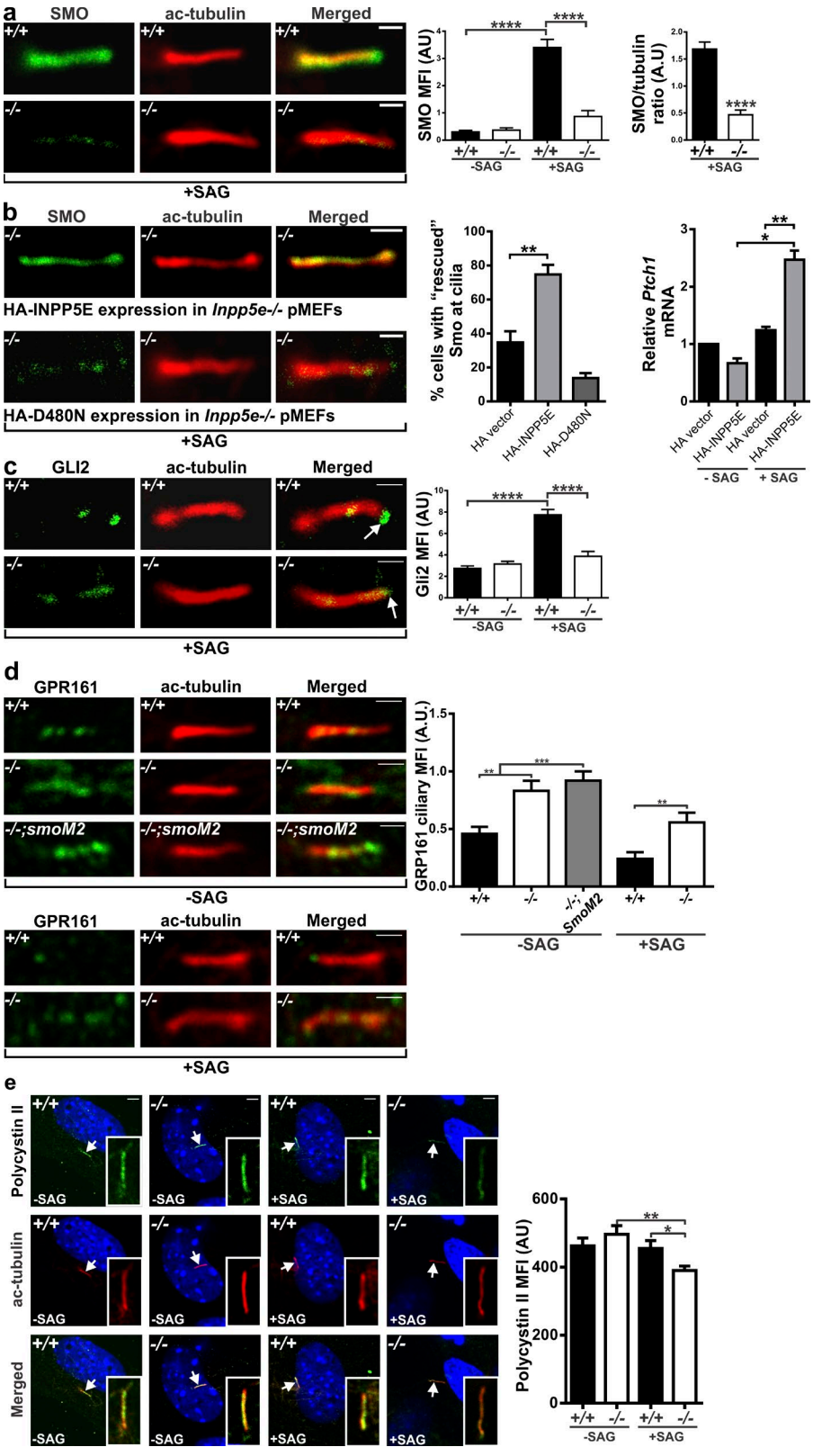

Figure 3. **INPP5E 5-phosphatase catalytic activity is essential for the cilia accumulation of Hh signaling components.** (a) *Inpp5e*$^{+/+}$ (*+/+*) and *Inpp5e*$^{-/-}$ (*−/−*) pMEFs, either untreated (not depicted but quantified) or SAG treated (+SAG), were fixed, permeabilized, and costained with smoothened (SMO) and acetylated α-tubulin (ac-tubulin) antibodies and imaged using confocal microscopy. The proximal and distal end of the cilium is orientated left to right, respectively, and was determined using γ-tubulin or pericentrin antibodies (not depicted). Bars, 500 nm. (graphs) The mean fluorescence intensity (MFI) of SMO along the axoneme (SMO MFI, left) and the SMO to ac-tubulin ratio at cilia (SMO/tubulin ratio, right) was measured in untreated (−SAG) and SAG-treated (+SAG) *Inpp5e*$^{+/+}$ and *Inpp5e*$^{-/-}$ pMEFs. Bars represent mean ± SEM. n = 3 pMEF lines per genotype, >100 cells per genotype; ***, P < 0.005; ****, P < 0.0001. (b) *Inpp5e*$^{-/-}$ (*−/−*) pMEFs transiently expressing either HA vector (not depicted), wild-type HA-INPP5E (HA-INPP5E), or phosphatase-dead HA-INPP5E^{D480N} (HA-D480N) were SAG treated (+SAG), fixed, permeabilized, and costained with SMO, ac-tubulin, and HA antibodies (HA staining not depicted) and imaged using confocal microscopy. The proximal and distal end of the cilium is orientated left to right, respectively. Bars, 500 nm. (left graph) The MFI of SMO along the axoneme was measured in transfected *Inpp5e*$^{-/-}$ pMEFs and classified as "rescued" when the SMO MFI reached >70% of wild-type levels (see Materials and methods). (right graph) RNA extracted from untreated (−SAG) or SAG-treated (+SAG) *Inpp5e*$^{-/-}$ (*−/−*) pMEFs transiently expressing either vector or HA-INPP5E was subjected to quantitative RT-PCR and normalized to *Gapdh*. The relative *Ptch1* transcript level was determined and normalized to *Inpp5e*$^{-/-}$ (*−/−*) pMEFs transiently expressing HA vector as 1. The transfection efficiency of *Inpp5e*$^{-/-}$ pMEFs was 81% ± 2.08% (SEM). Bars represent *Inpp5e*$^{-/-}$ pMEFs expressing vector (black bars), HA-INPP5E (light gray bars), or HA-D480N (dark gray bar), mean ± SEM. n = 3 transfections per pMEF line per genotype, >90 cells per genotype for immunofluorescence analysis. *, P < 0.05; **, P < 0.01; ***, P < 0.001. (c) *Inpp5e*$^{+/+}$ (*+/+*) and *Inpp5e*$^{-/-}$ (*−/−*) pMEFs either untreated (not depicted but quantified) or treated with SAG (+SAG) were fixed, permeabilized, and costained with GLI2 and ac-tubulin antibodies and imaged using confocal microscopy. The proximal and distal end of the cilium is orientated left to right, respectively. Bar, 500 nm. The MFI of GLI2 at the cilia tip (distal to the ac-tubulin signal indicated by arrow) in untreated (−SAG) and SAG-treated (+SAG) *Inpp5e*$^{+/+}$ and *Inpp5e*$^{-/-}$ pMEFs was measured. Bars represent mean ± SEM. n = 3 pMEF lines per genotype, >90 cells per genotype; ****, P < 0.0001. (d) *Inpp5e*$^{+/+}$ (*+/+*), *Inpp5e*$^{-/-}$ (*−/−*), or *Inpp5e*$^{+/+}$*;CMVCre;SmoM2* (*−/−;SmoM2*) pMEFs, either untreated (−SAG, top) or SAG treated (+SAG, bottom), were fixed, permeabilized, and costained with DAPI, and GPR161 and ac-tubulin antibodies and imaged using confocal microscopy. Bars, 500 nm. The MFI of GPR161 at the cilia axoneme was measured. Bar represents mean ± SEM, n = 2–4 pMEF lines per genotype, ~40 cells/genotype; *, P < 0.05; **, P < 0.01; ***, P < 0.001. (e) *Inpp5e*$^{+/+}$ (*+/+*) and *Inpp5e*$^{-/-}$ (*−/−*) pMEFs, either untreated (−SAG) or SAG treated (+SAG), were fixed, permeabilized, and costained with polycystin II and ac-tubulin antibodies and DAPI and imaged using confocal microscopy. Arrow indicates cilia. Bars, 500 nm. The MFI of polycystin II at cilia was measured in untreated (−SAG) and SAG-treated (+SAG) *Inpp5e*$^{+/+}$ and *Inpp5e*$^{-/-}$ pMEFs. Bars represent mean ± SEM. n = 3 pMEF lines per genotype, ~50 cells/genotype; **, P < 0.05; **, P < 0.01. AU, arbitrary units.

of PKD-2 in *cil-1* mutants, the closest *Caenorhabditis elegans* homologue of INPP5E (Bae et al., 2009). Also, although another recent study reports no change in polycystin II cilia localization with loss of *Inpp5e* (Garcia-Gonzalo et al., 2015), this study did not examine receptor localization after Hh pathway activation, the specific conditions under which the reduced polycystin II cilia localization was observed here in *Inpp5e*$^{-/-}$ pMEFs. We were unable to confidently measure FLAG-HTR6 intensity at cilia, as its expression in *Inpp5e*$^{-/-}$ pMEFs impacted ciliogenesis; however, reduced cilia enrichment of the receptor was observed in some ciliated cells with loss of *Inpp5e* (Fig. S3 c). We also evaluated the barrier function of the TZ to prevent the cilia entry of nonciliary proteins (Fig. S3 d). CEACAM-1 is a highly mobile plasma membrane glycoprotein that ectopically localizes to cilia in some models with loss of TZ barrier function (Chih et al., 2011; Francis et al., 2011). Recombinant GFP–CEACAM-1 was not detected at cilia in either *Inpp5e*$^{+/+}$ or *Inpp5e*$^{-/-}$ pMEFs irrespective of SAG treatment, suggesting *Inpp5e* deletion does not compromise the cilia entry barrier function of the TZ (Fig. S3 d). Collectively, these findings reveal loss of *Inpp5e* reduces the cilia accumulation of some cilia receptors specifically after Hh pathway activation via SAG but that cilia entry mechanisms remain intact.

INPP5E regulates phosphoinositide signals at the cilia TZ

The activation of Hh signaling in cultured cells promotes PI3K-dependent phosphorylation of AKT, suggesting pathway crosstalk (Riobó et al., 2006). However, whether Hh-mediated activation of PI3K, which in turn generates $PI(3,4,5)P_3$ via phosphorylation of $PI(4,5)P_2$, occurs locally at cilia is unknown. To this end, $PI(4,5)P_2$ and $PI(3,4,5)P_3$ cilia localization and their regulation by INPP5E and Hh signaling were examined using established immunocytochemical techniques that preserve organelle membranes and validated antibodies specific to $PI(4,5)P_2$ or $PI(3,4,5)P_3$ (Hammond et al., 2006, 2009; Yip et al., 2008). $PI(4,5)P_2$ localizes to the proximal end of cilia in SV40-transformed MEFs, *C. elegans*, and *Drosophila melanogaster*; however, the discrete distribution of $PI(4,5)P_2$ to cilia subdomains via colocalization with cilia domain markers has not been reported (Garcia-Gonzalo et al., 2015; Jensen et al., 2015; Park et al., 2015). Here, $PI(4,5)P_2$ was enriched proximal to the axoneme at the cilia base in untreated *Inpp5e*$^{+/+}$ pMEFs and was also distributed at low levels along the axoneme and colocalized with ac-tubulin (Figs. 4 a and S4 a). At the cilia base, $PI(4,5)P_2$ discretely localized between ac-tubulin and pericentrin (Fig. S4 b) and showed a similar distribution in hTERT retinal pigment epithelial (RPE) cells (Fig. S4 c, top), where it colocalized with the TZ marker TCTN1 (Fig. S4 c, middle; Garcia-Gonzalo et al., 2011). Notably colocalization of HA-INPP5E with TCTN1 revealed that in addition to localizing to the cilia axoneme, the 5-phosphatase partially localizes to the TZ in a subset of cells thereby in proximity to its substrate $PI(4,5)P_2$ (Fig. S4 c, bottom). At steady state, *Inpp5e*$^{-/-}$ pMEFs showed a $PI(4,5)P_2$ distribution similar to wild type (Figs. 4 a and S4 a), with a comparable signal intensity (MFI) at the TZ (Fig. 4 b) and $PI(4,5)P_2$ to ac-tubulin ratio (Fig. S4 d). However, at the axoneme, $PI(4,5)P_2$ intensity was modestly increased with *Inpp5e* deletion, consistent with previous studies (Fig. 4 b; Garcia-Gonzalo et al., 2015). In control studies, treatment of *Inpp5e*$^{+/+}$ pMEFs after cell fixation with neomycin, which binds and sequesters this $PI(4,5)P_2$ (Liscovitch et al., 1991), attenuated cilia-associated $PI(4,5)P_2$ signals (Fig. S4 e). In nonciliated cells after growth factor stimulation, plasma membrane $PI(4,5)P_2$ signals decrease because of its cleavage by phospholipase C and/or PI3K-mediated phosphorylation of $PI(4,5)P_2$, generating $PI(3,4,5)P_3$; however, the dynamics of $PI(4,5)P_2$ at cilia in response to agonist stimulation has not been reported (Balla, 2013). After SAG treatment of *Inpp5e*$^{+/+}$ pMEFs the number of $PI(4,5)P_2$-positive cilia (Fig. 4 c) and the MFI of $PI(4,5)P_2$ at the TZ was reduced, but axoneme $PI(4,5)P_2$ intensity slightly increased (Fig. 4 b). As an additional readout of the relative TZ $PI(4,5)P_2$ signal per cilia, the $PI(4,5)P_2$/ac-tubulin ratio was measured and was also reduced compared with untreated wild-type pMEFs (Fig. S4 d). Therefore, $PI(4,5)P_2$ signals decrease at the TZ but increase along the axoneme after SAG treatment of *Inpp5e*$^{+/+}$ pMEFs. The number of $PI(4,5)P_2$-positive cilia was unchanged after SAG treatment of *Inpp5e*$^{-/-}$ pMEFs (Fig. 4 c). $PI(4,5)P_2$ intensity at the TZ decreased in *Inpp5e*$^{-/-}$ pMEFs after SAG treatment but was increased relative to wild-type (Fig. 4, a and b; and Fig. S4 d). In addition SAG treatment of *Inpp5e*$^{-/-}$ pMEFs resulted in a loss of axoneme $PI(4,5)P_2$ signals (Fig. 4, a and b; and Fig. S4 a). Therefore with *Inpp5e* deletion $PI(4,5)P_2$ signals are increased after activation of Hh signaling.

INPP5E is a potent $PI(3,4,5)P_3$ 5-phosphatase in vitro and in vivo (Kisseleva et al., 2000; Hakim et al., 2016) but $PI(3,4,5)P_3$ has not been identified at cilia. Endogenous $PI(3,4,5)P_3$ and ac-tubulin costaining revealed that ∼50% of *Inpp5e*$^{+/+}$ pMEFs showed $PI(3,4,5)P_3$ at the cilia base (Fig. 4, d and e; and Fig. S4, f and g). $PI(3,4,5)P_3$ also localized to the cilia base in RPE cells (Fig. S4 h, top), with an intervening distribution between the axoneme and pericentrin (Fig. S4 g). In addition, $PI(3,4,5)P_3$ colocalized with the TZ marker, TCTN1 (Fig. S4 h, bottom), analogous to our findings for $PI(4,5)P_2$ (Fig. S4 c, bottom). The number of $PI(3,4,5)P_3$-positive cilia was increased in *Inpp5e* null pMEFs (Fig. 4 e), as was the TZ $PI(3,4,5)P_3$ intensity (Fig. 4 f) and TZ $PI(3,4,5)P_3$/ac-tubulin ratio (Fig. S4 i) relative to wild-type cells. After SAG treatment of *Inpp5e*$^{+/+}$ and *Inpp5e*$^{-/-}$ pMEFs, $PI(3,4,5)P_3$ was detected at the TZ (Fig. 4 d) of all cilia (Fig. 4 e), and the TZ $PI(3,4,5)P_3$ intensity (Fig. 4 f) and TZ $PI(3,4,5)P_3$/ac-tubulin ratio were increased in both genotypes compared with their respective untreated controls (Fig. S4 i) and were significantly higher in *Inpp5e* null cells (Figs. 4 f and S4 i). Therefore, activation of Hh signaling increases $PI(3,4,5)P_3$ signals at the TZ in wild-type and *Inpp5e*$^{-/-}$ pMEFs, and the relative $PI(3,4,5)P_3$ signal intensity was further increased with *Inpp5e* deletion (Figs. 4 f and S4 i). In control studies, PI3K inhibitor (LY294003) treatment reduced $PI(3,4,5)P_3$ signals at the cilia base in SAG-stimulated *Inpp5e*$^{+/+}$ pMEFs (Fig. S4 j). Additionally the fidelity of $PI(3,4,5)P_3$ and $PI(4,5)P_2$ immunostaining was further confirmed by colocalizing the endogenous lipid species with transfected GFP-Btk or GFP-PLC biosensors, which detect $PI(3,4,5)P_3$ and $PI(4,5)P_2$, respectively (Balla, 2013; Fig. S4, k and l). In summary, these findings show that INPP5E partially localizes to the TZ in proximity to its substrates, and with *Inpp5e* deletion, both $PI(4,5)P_2$ and $PI(3,4,5)P_3$ signals are increased after Hh pathway activation. A schematic of the relative $PI(4,5)P_2$ and $PI(3,4,5)P_3$ signal intensity at the TZ of *Inpp5e*$^{+/+}$ and *Inpp5e*$^{-/-}$ pMEFs in the presence or absence of SAG is shown in Fig. S4 m. Collectively, this analysis reveals that $PI(4,5)P_2$ and $PI(3,4,5)P_3$ signals are enriched at the TZ and are differentially and dynamically regulated by Hh signaling and INPP5E.

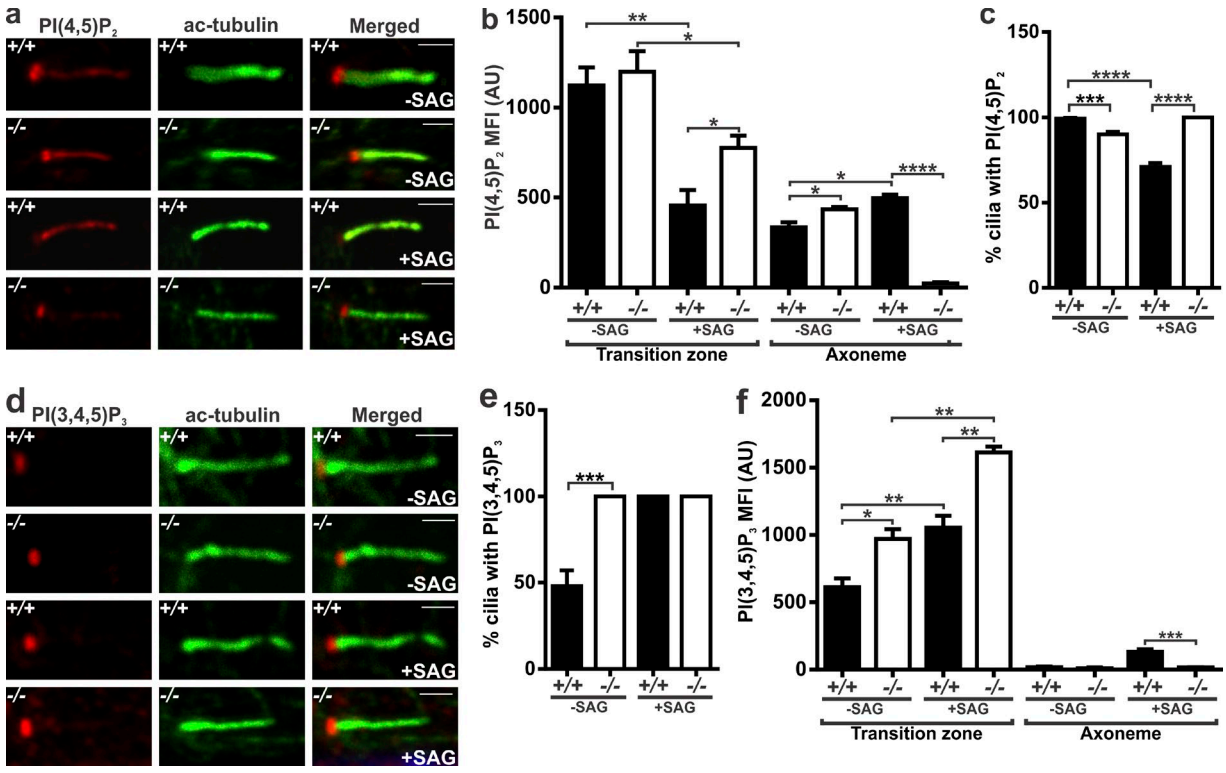

Figure 4. **PI(4,5)P_2 and PI(3,4,5)P_3 localize to the cilia TZ and are regulated by INPP5E and Hh signaling.** (a) *Inpp5e*$^{+/+}$ (+/+) and *Inpp5e*$^{-/-}$ (−/−) pMEFs, either untreated (−SAG) or SAG treated (+SAG), were fixed, permeabilized, and costained with PI(4,5)P_2 and acetylated α-tubulin (ac-tubulin) antibodies and imaged using confocal microscopy. The proximal and distal end of the cilium is orientated left to right, respectively. Bars, 500 nm. (b) *Inpp5e*$^{+/+}$ (+/+) and *Inpp5e*$^{-/-}$ (−/−) pMEFs, either untreated (−SAG) or SAG treated (+SAG), were costained with PI(4,5)P_2 and ac-tubulin antibodies as in panel a. The MFI of PI(4,5)P_2 at the cilia "transition zone" or "axoneme" was measured. Bars represent mean ± SEM. *n* = 3 pMEF lines per genotype, ∼60 cells/genotype; *, P < 0.05; **, P < 0.01; ***, P < 0.005; ****, P < 0.0001. (c) *Inpp5e*$^{+/+}$ (+/+) and *Inpp5e*$^{-/-}$ (−/−) pMEFs, either untreated (−SAG) or SAG treated (+SAG), were costained with PI(4,5)P_2 and ac-tubulin antibodies as in panel a. The percentage of ac-tubulin–positive cilia that were also positive for PI(4,5)P_2 was scored. Bars represent mean ± SEM. *n* = 3 pMEF lines/genotype, ∼60 cells/genotype; ***, P < 0.001; ****, P < 0.0001. (d) *Inpp5e*$^{+/+}$ (+/+) and *Inpp5e*$^{-/-}$ (−/−) pMEFs, either untreated (−SAG) or SAG treated (+SAG), were fixed, permeabilized, and costained with PI(3,4,5)P_3 and acetylated α-tubulin (ac-tubulin) antibodies and imaged using confocal microscopy. The proximal and distal end of the cilium is orientated left to right, respectively. Bars, 500 nm. (e) *Inpp5e*$^{+/+}$ (+/+) and *Inpp5e*$^{-/-}$ (−/−) pMEFs either untreated (−SAG) or SAG treated (+SAG) were costained with PI(3,4,5)P_3 and acetylated α-tubulin antibodies as in panel d. (e) The percentage of ac-tubulin–positive cilia that were also positive for PI(3,4,5)P_3 was scored. Bars represent mean ± SEM. *n* = 3 pMEF lines per genotype, ∼60 cells per genotype; ***, P < 0.005. (f) *Inpp5e*$^{+/+}$ (+/+) and *Inpp5e*$^{-/-}$ (−/−) pMEFs, either untreated (−SAG) or SAG treated (+SAG), were costained with PI(3,4,5)P_3 and ac-tubulin antibodies as in panel d. The MFI of PI(3,4,5)P_3 at the cilia TZ or axoneme was measured. Bars represent mean ± SEM. *n* = 3 pMEF lines per genotype, ∼60 cells/genotype; *, P < 0.05; **, P < 0.01; ***, P < 0.005. AU, arbitrary units.

INPP5E regulates the molecular organization of the cilia TZ

Emerging evidence suggests a subset of ciliopathies, including Meckel–Gruber and JBTS, arise from dysfunction of the TZ, resulting in aberrant cilia signaling (Hu et al., 2010; Chih et al., 2011; Garcia-Gonzalo et al., 2011; Sang et al., 2011; Williams et al., 2011). Several ciliopathy proteins such as MKS1, B9D proteins, and Tectonic module components localize to the TZ and modulate TZ function via scaffold assembly (Chih et al., 2011; Garcia-Gonzalo et al., 2011; Sang et al., 2011; Williams et al., 2011; Roberson et al., 2015). The TZ is essential for cilia compartmentalization and regulates the ciliary membrane composition of signaling receptors via modulating cilia retention and/or cilia entry mechanisms. Disruption of TZ function via depletion of scaffolding proteins that localize to the TZ results in the reduced ciliary enrichment of signaling proteins such as SMO, associated with impaired signal transduction, reminiscent of our findings here in *Inpp5e*$^{-/-}$ pMEFs (Chih et al., 2011; Lambacher et al., 2016). Interestingly, many TZ scaffolding proteins contain protein modules predicted to bind PIs such as PI(4,5)P_2 and PI(3,4,5)P_3 (Arts et al., 2007; Delous et al., 2007; Williams et al., 2011; Jensen et al., 2015), an event that may influence their localization to the TZ. Therefore, we examined whether the increased PI(4,5)P_2 and PI(3,4,5)P_3 signals at the TZ of Hh-stimulated *Inpp5e*$^{-/-}$ pMEFs were associated with mislocalization of TZ scaffolding proteins.

ARL13B is mutated in JBTS and is necessary for INPP5E cilia localization (Humbert et al., 2012); however, whether INPP5E plays in a role in ARL13B cilia localization is unknown. ARL13B localizes along the cilia axoneme; however, in MKS1 or B9, complex reduction-of-function mutants with reduced TZ function, ARL13B is partially redirected to the TZ (Cevik et al., 2013). In both untreated and SAG-treated *Inpp5e*$^{+/+}$ and *Inpp5e*$^{-/-}$ pMEFs, endogenous ARL13B was detected along the axoneme (Fig. 5 a). However, in the majority of SAG-treated *Inpp5e*$^{-/-}$ pMEFs ARL13B was also detected at the cilia base, consistent with partial localization at the TZ, suggesting TZ function may be compromised in *Inpp5e*$^{-/-}$ pMEFs after Hh pathway activation (Fig. 5 a arrow).

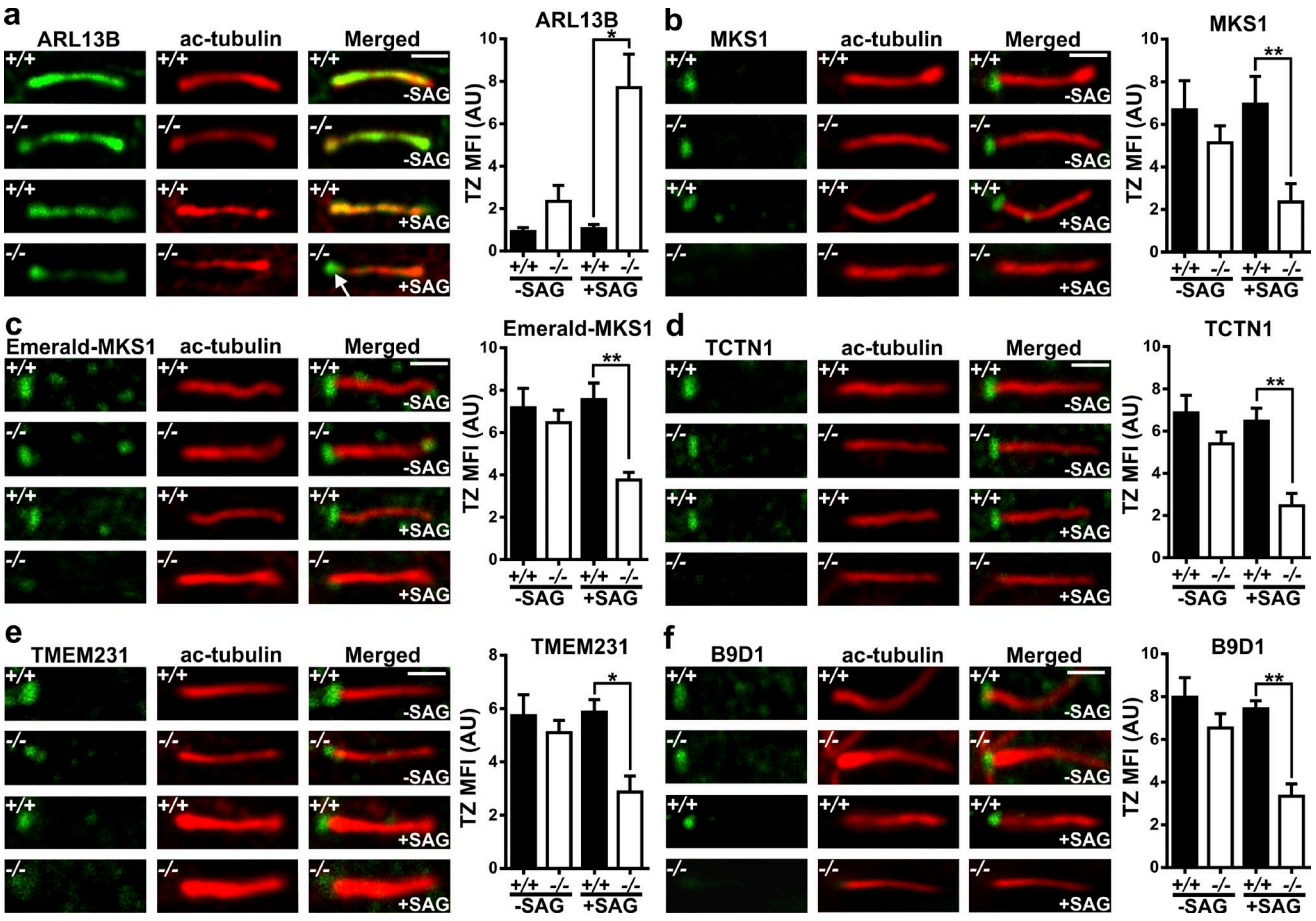

Figure 5. **INPP5E regulates the molecular organization of the cilia TZ.** (a) *Inpp5e*$^{+/+}$ (+/+) and *Inpp5e*$^{-/-}$ (−/−) pMEFs either untreated (−SAG) or SAG treated (+SAG) were fixed, permeabilized and costained with ARL13B and acetylated α-tubulin (ac-tubulin) antibodies and imaged using confocal microscopy. The proximal and distal end of the cilium is orientated left to right, respectively. Bar, 500 nm. Arrow indicates ectopic ARL13B localization. The MFI of ARL13B at the transition zone (TZ MFI) was measured. Bars represent mean ± SEM. n = 3 pMEF lines per genotype, ~60 cells per genotype; *, $P < 0.05$. (b) *Inpp5e*$^{+/+}$ (+/+) and *Inpp5e*$^{-/-}$ (−/−) pMEFs, either untreated (−SAG) or SAG treated (+SAG), were fixed, permeabilized, and costained with MKS1 and acetylated α-tubulin (ac-tubulin) antibodies and imaged using confocal microscopy. The proximal and distal end of the cilium is orientated left to right, respectively. Bar, 500 nm. The MFI of the respective TZ component at the TZ was measured. Bars represent mean ± SEM. n = 3 pMEF lines per genotype, ~60 cells per genotype; **, $P < 0.01$. (c) *Inpp5e*$^{+/+}$ (+/+) and *Inpp5e*$^{-/-}$ (−/−) pMEFs transfected with Emerald-MKS1 were either untreated (−SAG) or SAG treated (+SAG), fixed, permeabilized, stained with ac-tubulin antibodies, and imaged using confocal microscopy. The proximal and distal end of the cilium is orientated left to right, respectively. Bar, 500 nm. The MFI of Emerald-MKS1 at the TZ was measured (TZ MFI). Bars represent mean ± SEM. n = 3 pMEF lines per genotype, ~60 cells per genotype; **, $P < 0.01$. (d–f) *Inpp5e*$^{+/+}$ (+/+) and *Inpp5e*$^{-/-}$ (−/−) pMEFs, either untreated (−SAG) or SAG treated (+SAG), were fixed, permeabilized, and costained with TCTN1 (d), TMEM231 (e), or B9D1 (f) and ac-tubulin and imaged using confocal microscopy. The proximal and distal end of the cilium is orientated left to right, respectively. Bar, 500 nm. The MFI of the respective TZ component at the transition zone (TZ MFI) was measured. Bars represent mean ± SEM. n = 3 pMEF lines per genotype, ~60 cells per genotype; *, $P < 0.05$; **, $P < 0.01$. AU, arbitrary units.

To assess TZ composition with *Inpp5e* deletion, the localization of several TZ components was evaluated at steady state (−SAG) and after Hh pathway activation via SAG (+SAG; Fig. 5, b–f). The Tectonic TZ component TCTN1 interacts with MKS1 and B9D1. TCTN1 is required for the TZ localization of B9D1 and TMEM231 and together with other TZ components cooperatively regulates TZ function (Chih et al., 2011; Garcia-Gonzalo et al., 2011; Williams et al., 2011; Szymanska and Johnson, 2012). Endogenous MKS1 (and recombinant Emerald-MKS1), TCTN1, TMEM231, and B9D1 localized to the TZ at steady state in *Inpp5e*$^{+/+}$ and *Inpp5e*$^{-/-}$ pMEFs and in SAG-treated *Inpp5e*$^{+/+}$ pMEFs but showed reduced or absent TZ localization in SAG-treated *Inpp5e*$^{-/-}$ pMEFs, consistent with the contention that *Inpp5e* ablation impairs the TZ localization of scaffolding proteins after Hh pathway activation (Fig. 5, b–f). In control studies endogenous MKS1, TCTN1, B9D1, and TMEM231 colocalized with recombinant MKS1 (Fig. S5 a). Septins form a diffusion barrier in budding yeast and in mammalian cells play a scaffolding role (Mostowy and Cossart, 2012). At cilia, septins form a SEPT2–SEPT5–SEPT7 complex and localize at the cilia base and along the axoneme, where they regulate ciliogenesis and cilia length (Ghossoub et al., 2013). At the cilia base, septins are proposed to form a diffusion barrier separating the cilia and plasma membranes, and SEPT2 facilitates the cilia retention of receptors, including SMO and HTR6, after Hh pathway activation (Hu et al., 2010). In addition, SEPT2 is required for the TZ localization of some B9 complex components (Garcia-Gonzalo et al., 2011). The mechanisms mediating the cilia localization of septins is unknown; however, septins interact with several PIs, including the INPP5E substrates $PI(4,5)P_2$ and $PI(3,4,5)P_3$ (Mostowy and Cossart, 2012). The role of PIs in septin function is complex, as various PIs regulate septin localization and oligomerization, often in a concentration-dependent manner. Some studies suggest

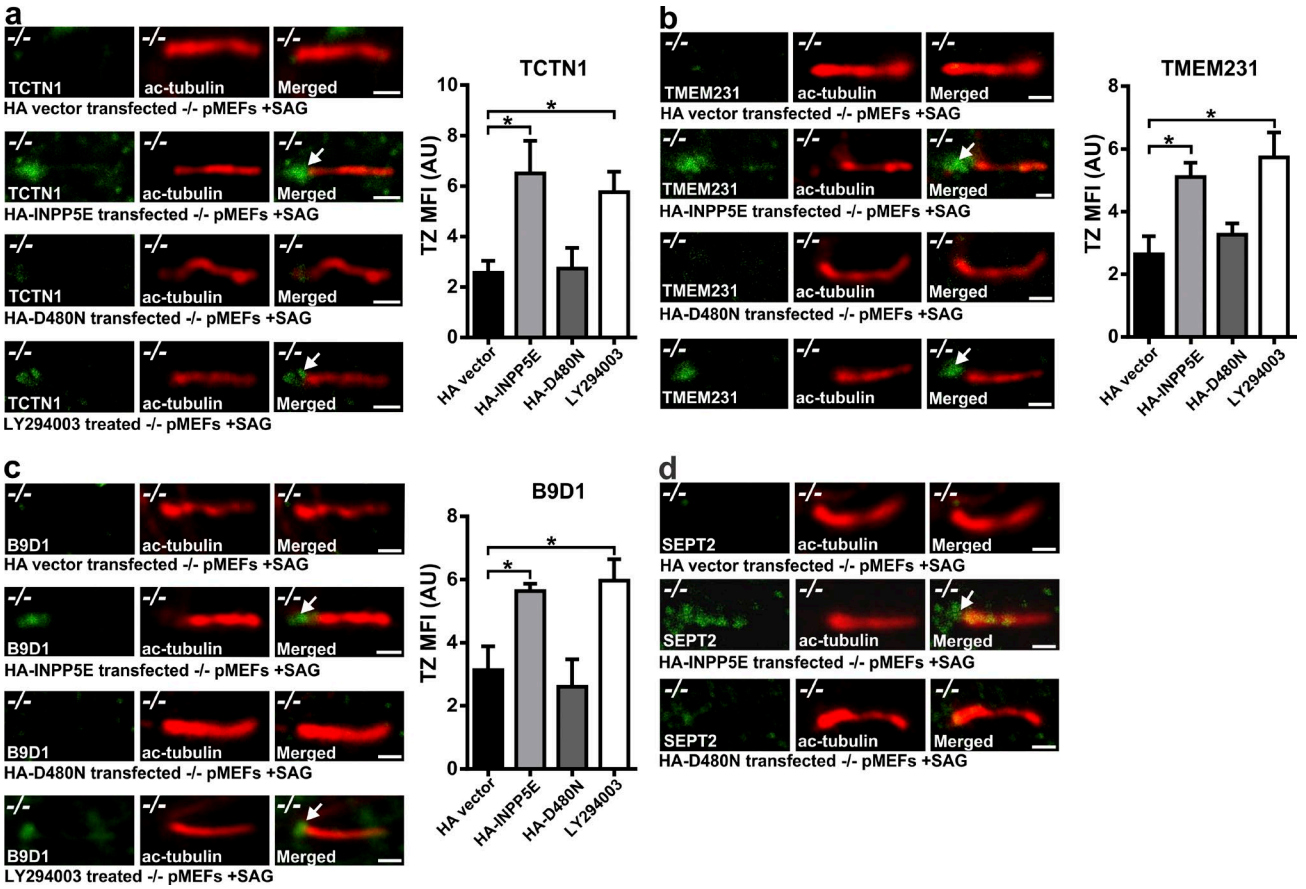

Figure 6. **INPP5E 5-phosphatase activity regulates the molecular organization of the cilia TZ.** (a–c) *Inpp5e*$^{-/-}$ (−/−) pMEFs transiently expressing HA vector (top), wild-type HA-INPP5E (HA-INPP5E, second panel), phosphatase-dead HA-INPP5E^{D480N} (HA-D480N, third panel) or mock transfected and treated with LY294003 (PI3-kinase inhibitor, fourth panel) were SAG treated (+SAG), fixed, permeabilized, and costained with TCTN1 (a), TMEM231 (b), or B9D1(c) antibodies and acetylated α-tubulin (ac-tubulin) and HA antibodies (HA staining to detect transfected cells is not depicted) and imaged using confocal microscopy. The proximal and distal ends of the cilium are orientated left to right, respectively. Arrow indicates TZ localization. Bars, 500 nm. The MFI of TCTN1(a), TMEM231 (b), or B9D1 (c) at the transition zone (TZ MFI) was measured in *Inpp5e*$^{-/-}$ pMEFs expressing HA vector (black bars), HA-INPP5E (light gray bars), HA-D480N (dark gray bars), and mock transfected with LY294003 treatment (white bars). Bars represent mean ± SEM. n = 3 transfections, ∼50 cells per condition; *, $P < 0.05$. (d) *Inpp5e*$^{-/-}$ (−/−) pMEFs transiently expressing HA vector (top), wild-type HA-INPP5E (HA-INPP5E, second panel), or phosphatase-dead HA-INPP5E^{D480N} (HA-D480N, third panel) were SAG treated (+SAG), fixed, permeabilized, and costained with SEPT2, ac-tubulin and HA antibodies (HA staining to detect transfected cells is not depicted) and imaged using confocal microscopy. The proximal and distal ends of the cilium are orientated left to right, respectively. Arrow indicates cilia base. Bars, 500 nm. AU, arbitrary units.

septins preferentially bind and assemble on membranes with low $PI(4,5)P_2$, whereas other studies propose high $PI(4,5)P_2$ is preferred (Maléth et al., 2014; Badrane et al., 2016). In steady-state wild-type and *Inpp5e*$^{-/-}$ pMEFs, SEPT2 localized at the axoneme and cilia base (Fig. S5 b, arrows), as reported previously (Hu et al., 2010; Ghossoub et al., 2013). SEPT2 cilia distribution was largely unchanged in *Inpp5e*$^{+/+}$ pMEFs after SAG stimulation; however, in SAG-treated *Inpp5e*$^{-/-}$ pMEFs, SEPT2 localization at the cilia base was reduced, with only low level SEPT2 puncta at the axoneme observed (Fig. S5 b). Collectively, the mislocalization of TCTN1, MKS1, TMEM231, B9D1, and SEPT2 from the TZ in *Inpp5e* null cells after Hh pathway activation is consistent with a compromised TZ.

To determine whether the INPP5E-mediated degradation of $PI(4,5)P_2$ and $PI(3,4,5)P_3$ was critical for the normal assembly of scaffolding proteins at the TZ in the response to Hh signaling, *Inpp5e*$^{-/-}$ pMEFs were reconstituted with wild-type or catalytically inactive INPP5E. Expression of HA-INPP5E, but not phosphatase-dead HA-INPP5E^{D480N} or vector controls, in *Inpp5e*$^{-/-}$ pMEFs restored the TZ localization of TCTN1, TMEM231, and B9D1 (Fig. 6, a–c) and the cilia recruitment of SEPT2 (Fig. 6 d) after SAG stimulation. Additionally, PI3K inhibition using LY294003 rescued the mislocalization of TCTN1, TMEM231, and B9D1 in SAG-treated *Inpp5e*$^{-/-}$ pMEFs (Fig. 6, a–c), suggesting local $PI(3,4,5)P_3$ signaling contributes to TZ component localization. These studies suggest INPP5E 5-phosphatase regulation of the phosphoinositide composition at the TZ is essential for the correct localization of TZ components.

INPP5E regulates the function of the cilia TZ

The TZ has various functions, including cilia and cytosol compartmentalization via excluding the cilia entry of noncilia proteins. The TZ also acts to retain cilia receptors after Hh pathway activation to allow cilia receptor accumulation (Hu et al., 2010; Chih et al., 2011). The function of the TZ can be assessed experimentally by live-cell imaging of cilia-localized receptors after photobleaching (Hu et al., 2010; Chih et al., 2011). Knockdown of TZ components, including *B9d1* and *Tmem231*

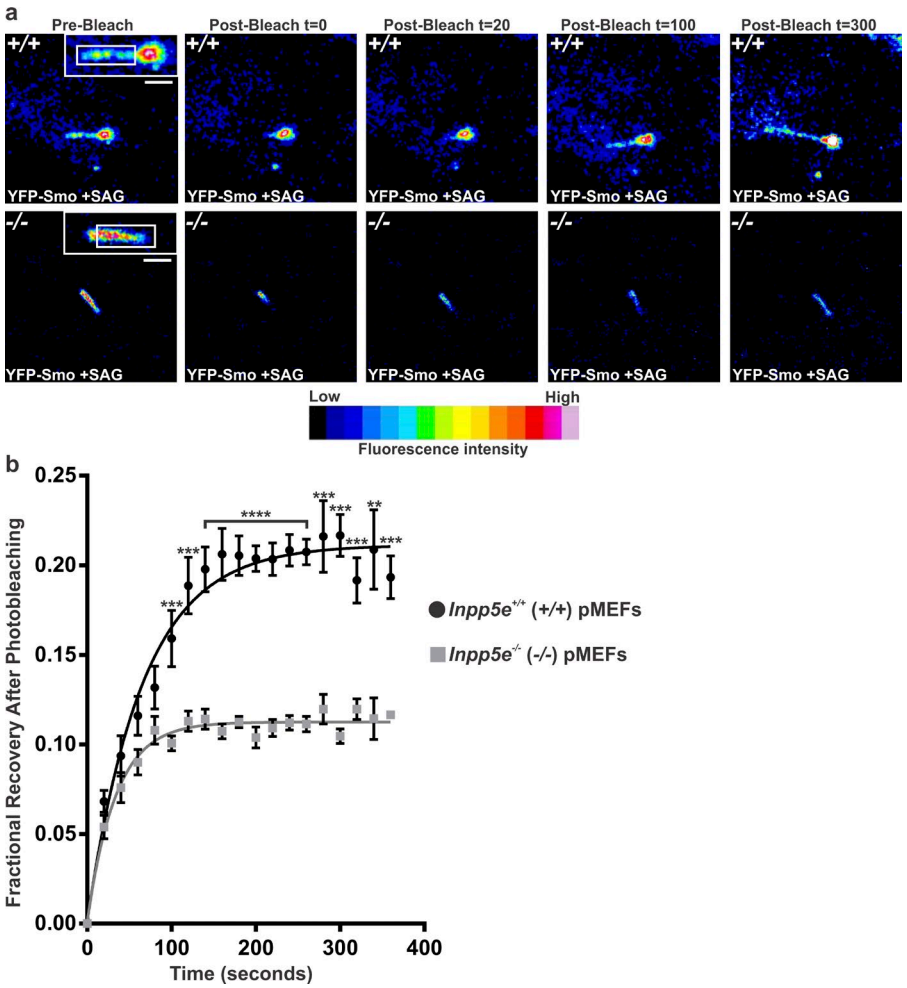

Figure 7. **INPP5E regulates TZ function.** (a and b) *Inpp5e*$^{+/+}$ (+/+) and *Inpp5e*$^{-/-}$ (−/−) pMEFs transiently expressing YFP-SMO were SAG treated (+SAG), and cilia with adequate and comparable YFP-SMO signal were selected for FRAP analysis. (a) Ciliary YFP-SMO signal intensity is shown before bleaching (Pre-Bleach), immediately after bleaching (t = 0), and at t = 20, t = 100, and t = 300 s after bleaching. Image has been pseudocolored with a graded fluorescence signal. Inset shows region of photobleached YFP-SMO ciliary signal (~90% of YFP-SMO signal). The boxed area in the inset image shows the area that was photobleached. Bars, 1.5 µm. (b) The fractional recovery of YFP-SMO after photobleaching was measured. Bars represent mean ± SEM. Circles (black) and squares (gray) represent ciliary YFP-SMO FRAP in *Inpp5e*$^{+/+}$ and *Inpp5e*$^{-/-}$ pMEFs, respectively. Four primary MEF cell lines per genotype were independently transfected, and two or three cells per transfection were analyzed, for a total of 10 cilia per genotype. *, P < 0.05; **, P < 0.01; ***, P < 0.005; ****, P < 0.0001.

or *Sept2* depletion, have shown TZ dysfunction experimentally by increased FRAP of ciliary receptors compared with controls after Hh pathway activation (Hu et al., 2010; Chih et al., 2011). To investigate the regulation of SMO dynamics at cilia by INPP5E, *Inpp5e*$^{+/+}$ and *Inpp5e*$^{-/-}$ pMEFs were transfected with YFP-tagged SMO (YFP-SMO; Kroeze et al., 2015) to allow for detection of fluorescently labeled SMO in live cells stimulated with SAG to activate Hh signaling and thereby induce YFP-SMO accumulation at cilia. Recombinant YFP-SMO showed reduced cilia localization in ~50% of *Inpp5e*$^{-/-}$ pMEFs (unpublished data); however, for the FRAP analysis, *Inpp5e*$^{-/-}$ cells with YFP-SMO cilia intensities similar to wild type were selected (Fig. 7 a). The recovery of YFP-SMO at cilia was assessed in SAG-treated *Inpp5e*$^{+/+}$ versus *Inpp5e*$^{-/-}$ pMEFs via FRAP, which measures the bidirectional movement of the receptor through the TZ (Fig. 7). At time 0 min, ~90% of the ciliary YFP-SMO signal (Fig. 7 a, boxed regions in inset) was bleached, with 10% of the YFP-SMO signal retained to allow Z-position tracking of the cilium. YFP-SMO recovery was measured for 400 s after photobleaching and the cilia fluorescence to cytoplasmic fluorescence ratio (Fcilia/c) determined over time (Fig. 7 b). Data were expressed as fractional recovery of Fcilia/c, where each postbleach time point was divided by the mean prebleach Fcilia/c value and then normalized to time 0 min (see Materials and methods). The FRAP of YFP-SMO was comparable between genotypes for the first 100 s, after which time recovery plateaued in *Inpp5e*$^{+/+}$ pMEFs (Fig. 7, a and b). However, in *Inpp5e*$^{-/-}$ pMEFs, YFP-SMO FRAP increased over time compared with *Inpp5e*$^{+/+}$, suggesting ongoing and continued exchange of the YFP-SMO ciliary signal consistent with a loss in the ciliary retention of YFP-SMO (Hu et al., 2010). These studies reveal INPP5E is essential for TZ function after Hh pathway activation (Fig. 7, a and b).

Discussion

Ciliopathies arise because of cilia dysfunction and aberrant cilia-mediated signal transduction (Waters and Beales, 2011). *INPP5E* is mutated in JBTS, and its ablation in mice leads to ciliopathy phenotypes by molecular mechanisms that are still emerging (Jacoby et al., 2009; Chávez et al., 2015; Garcia-Gonzalo et al., 2015). Recent studies using immortalized *Inpp5e*$^{\Delta/\Delta}$ MEFs suggests INPP5E regulates the ciliary level of the Hh suppressor GPR161 via TULP3, that in turn promotes GLI3R formation and reduced Hh signaling (Mukhopadhyay et al., 2013; Garcia-Gonzalo et al., 2015). Here, we reveal *Inpp5e* ablation suppresses Hh signaling associated with aberrant Hh-dependent embryonic patterning in vivo including reduced "high level" and expansion of "intermediate level" Hh signaling. We investigated the mechanisms leading to the loss of high-level Hh signaling with *Inpp5e* deletion, and our genetic studies provide evidence that INPP5E contributes to Hh signaling regulation during embryonic development and that perturbation of

this pathway underlies several disease phenotypes associated with *Inpp5e* deletion. Anophthalmia is typically associated with repressed Hh signaling (Bakrania et al., 2010) and was observed in all *Inpp5e*$^{-/-}$ embryos at E15.5. Rescue of the anophthalmia in *Inpp5e*$^{-/-}$*;CMVCre;SmoM2* embryos suggests SMOM2 expression in the context of *Inpp5e* deletion reequilibrates Hh signaling in vivo (Bakrania et al., 2010; Slavotinek, 2011). Supporting this, we observed normalization of Hh target gene expression in *Inpp5e*$^{-/-}$*;CMVCre;SmoM2* embryos. Notably, GPR161 cilia levels were increased in rescue *Inpp5e*$^{-/-}$*;CMVCre;SmoM2* pMEFs, suggesting the partial phenotypic rescue is independent of the cilia regulation of GPR161. However, the persistence of some *Inpp5e* null phenotypes with SMOM2 expression may be a consequence of increased GPR161 at cilia, and thus, the deregulation of SMO and GPR161 at cilia may additively impact the in vivo phenotypes of *Inpp5e*$^{-/-}$ mice.

Inpp5e$^{-/-}$ embryos exhibit normal cilia number but reduced Hh signaling, suggesting a defect in the coordination of Hh signal transduction. We demonstrate INPP5E is essential for maximal SMO accumulation at cilia after the Hh pathway; however, some *Inpp5e* null cells showed low-level SMO cilia accumulation, suggesting some modes of SMO trafficking are intact. We propose a defect in cilia receptor retention may underlie the reduced cilia localization of SMO in *Inpp5e* null cells. Congruent with this, cilia entry is unperturbed with *Inpp5e* deletion, but the cilia accumulation of receptors, including SMO and polycystin II, is reduced specifically after Hh pathway activation. FRAP analysis revealed an increase in the cilia exchange of SMO in *Inpp5e*$^{-/-}$ pMEFs, collectively suggesting the barrier properties of the TZ that normally act to limit SMO diffusion out of the cilium are impaired with *Inpp5e* deletion. Importantly, we show the 5-phosphatase activity of INPP5E, which regulates the levels of $PI(4,5)P_2$ and $PI(3,4,5)P_3$ at the TZ, is essential for SMO accumulation at cilia as well as Hh signaling and that expression of constitutively active SMOM2 partially rescues *Inpp5e* null embryonic defects. Therefore, we propose the reduced cilia retention of SMO is at least in part responsible for some *Inpp5e*$^{-/-}$ phenotypes.

The TZ plays an essential role in the cilia accumulation of receptors; however, the molecular mechanisms underlying TZ function are still emerging. Several studies suggest the assembly of protein scaffolds at the TZ act as a proteinaceous gate that contributes to TZ barrier function, and other studies propose septins play a role (Hu et al., 2010; Chih et al., 2011; Garcia-Gonzalo et al., 2011; Huang et al., 2011; Williams et al., 2011; Roberson et al., 2015; Yang et al., 2015). In *C. elegans*, the recent identification of a ciliary zone of exclusion at the TZ has raised the possibility of a "lipid gate" barrier that also compartmentalizes signaling molecules at cilia (Jensen et al., 2015). We have demonstrated here that INPP5E partially localizes to the TZ, that its substrates $PI(4,5)P_2$ and $PI(3,4,5)P_3$ are enriched at the TZ, and that their levels turn over in response to Hh pathway activation. We propose $PI(4,5)P_2$ and $PI(3,4,5)P_3$ at the TZ contribute to the localization and thereby function of TZ scaffold components, which in turn maintain SMO at cilia. The protein scaffold components MKS1, TCTN1, TMEM231, and B9D1 cooperatively localize to the TZ, and SEPT2 localizes TMEM231 and B9D1 to the TZ, and all are essential for TZ function (Chih et al., 2011; Garcia-Gonzalo et al., 2011; Williams et al., 2011; Roberson et al., 2015). TMEM231 and TMEM17 may anchor B9 complex components, including TCTN1 and B9D1, to the TZ membrane and in this way act as a "protein fence" to limit diffusion of ciliary membrane proteins. Here, we show that Hh-stimulated, but not steady-state, *Inpp5e*$^{-/-}$ pMEFs exhibit reduced TZ localization of MKS1, TCTN1, TMEM231, and B9D1, which is associated with increased $PI(4,5)P_2$ and $PI(3,4,5)P_3$ signals at the TZ. Significantly, expression of wild-type, but not phosphatase-dead, INPP5E restored the localization of TZ scaffold components in Hh-stimulated *Inpp5e*$^{-/-}$ pMEFs, revealing INPP5E regulation of $PI(4,5)P_2$ and/or $PI(3,4,5)P_3$ signaling at the TZ contributes to TZ function. PIs are integral for the identity of cellular and organelle membranes as well as membrane microdomains, and they serve as compartment-specific recognition signals for the recruitment of transmembrane or cytosolic proteins (Carlton and Cullen, 2005). Many TZ components, including MKS1, TCTN1, and TMEM231, contain transmembrane domains and/or multiple modules such as coiled-coil, B9, and C2 domains that mediate their TZ localization and facilitate scaffold assembly (Arts et al., 2007; Delous et al., 2007; Williams et al., 2011; Jensen et al., 2015). Significantly, these protein modules are predicted to mediate PI binding or enhance protein–membrane or protein–protein avidity via coincidence detection (Nalefski and Falke, 1996; Lemmon, 2008; Jensen et al., 2015). Similarly, septins bind various PIs, and septin oligomerization that is integral to its TZ barrier function is regulated by PIs in a concentration-dependent manner (Casamayor and Snyder, 2003; Badrane et al., 2012; Bridges et al., 2014).

As shown here, the level of both $PI(4,5)P_2$ and $PI(3,4,5)P_3$ changes at the TZ after Hh pathway activation, raising the possibility that the $PI(4,5)P_2$/$PI(3,4,5)P_3$ signal ratio itself plays a role in TZ function. Indeed $PI(4,5)P_2$/$PI(3,4,5)P_3$ composition and ratio contributes to membrane identity and the targeting of proteins to other membrane subdomains (Heo et al., 2006). Interestingly, inhibition of PI3K in Hh-stimulated *Inpp5e* null pMEFs partially restored the TZ localization of TCTN1, TMEM231, and B9D1, suggesting a specific role for $PI(3,4,5)P_3$; however, further studies are required to determine the individual and/or cooperative roles of $PI(4,5)P_2$ and $PI(3,4,5)P_3$ in TZ molecular organization and function.

We showed that $PI(4,5)P_2$ and $PI(3,4,5)P_3$ signals are both modulated at the TZ by Hh signaling, whereby $PI(4,5)P_2$ signals decrease and $PI(3,4,5)P_3$ signals increase after Hh pathway activation. The simplest interpretation of this profile is that $PI(4,5)P_2$ is constitutively localized to the TZ in quiescent cells and with induction of Hh signaling PI3K is activated, allowing for $PI(4,5)P_2$ phosphorylation to generate $PI(3,4,5)P_3$, resulting in a concomitant decrease in $PI(4,5)P_2$ and increase in $PI(3,4,5)P_3$ signals. Our model proposes *Inpp5e* deletion amplifies Hh-stimulated changes in $PI(4,5)P_2$ and $PI(3,4,5)P_3$ signals at the TZ, resulting in misorganization and dysfunction of the TZ and reduced levels of SMO at cilia with suppression of GLI2 cilia tip localization, resulting in reduced Hh signaling (Fig. 8). Others have recently reported INPP5E regulates the cilia enrichment of the Hh suppressor GPR161, which is recruited to cilia via TULP3 that binds $PI(4,5)P_2$ (Mukhopadhyay et al., 2010; Chávez et al., 2015; Garcia-Gonzalo et al., 2015). In this way, increased axoneme $PI(4,5)P_2$ signals with *Inpp5e* deletion may enhance TULP3-mediated GPR161 cilia recruitment, which acts to suppress Hh signaling by promoting GLI3R formation (Mukhopadhyay et al., 2013; Garcia-Gonzalo et al., 2015). Here, we showed GPR161 is increased at cilia in a subpopulation of quiescent *Inpp5e*$^{-/-}$ pMEFs and that after Hh pathway activation, GPR161 is partially removed from cilia,

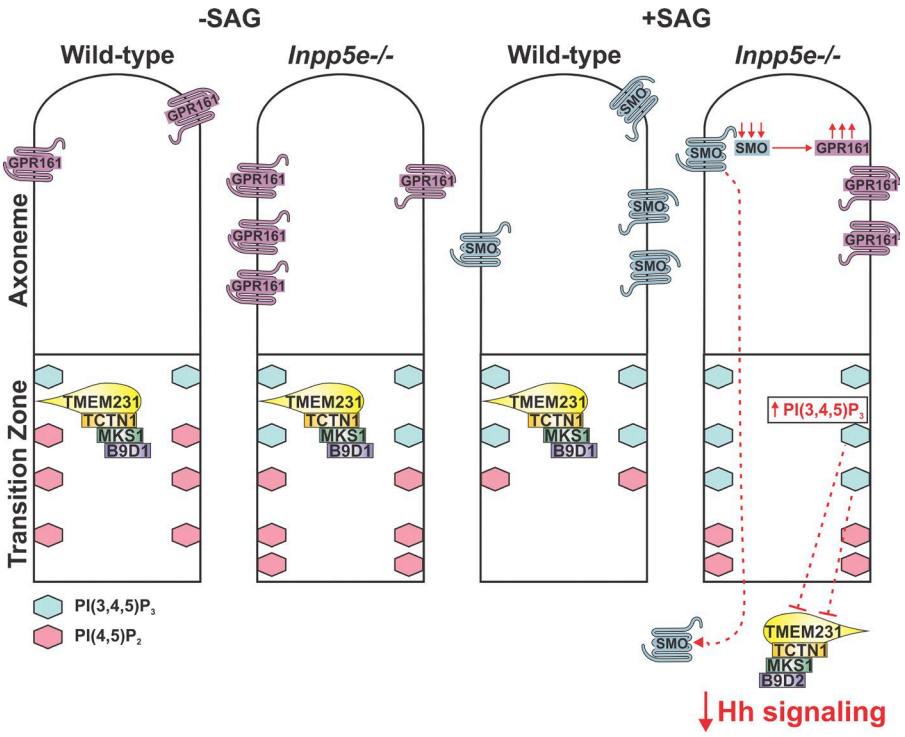

Figure 8. **Proposed model for the role INPP5E plays at cilia.** PI(4,5)P_2 (pink hexagons) and PI(3,4,5)P_3 signals (blue hexagons) localize to the cilia TZ. Protein scaffolds, including TMEM231, TCTN1, MKS1, and B9D1, localize to the TZ. In the absence of Hh pathway activation (–SAG), GPR161 levels at the cilia axoneme are increased in *Inpp5e*$^{-/-}$ pMEFs (Chávez et al., 2015; Garcia-Gonzalo et al., 2015). After Hh pathway activation (+SAG) of wild-type pMEFs, PI(4,5)P_2 signals decrease and PI(3,4,5)P_3 signals increase at the TZ, and SMO accumulates and is retained at cilia, which is associated with the exit of GPR161 from cilia (Pal et al., 2016). After Hh pathway activation (+SAG) of *Inpp5e*$^{-/-}$ pMEFs, PI(4,5)P_2 and PI(3,4,5)P_3 signals are disproportionately increased at the TZ (compared with wild type), which is associated with the mislocalization of TZ components TMEM231, TCTN1, MKS1, B9D1, and SEPT2 (latter not depicted), leading to the reduced accumulation and retention of SMO at cilia and thereby increased cilia axoneme levels of GPR161. Dashed arrows and lines are proposed pathways. Inhibition of PI3K-generated PI(3,4,5)P_3 signals restores the localization of TZ components to cilia in *Inpp5e*$^{-/-}$ pMEFs, suggesting a role for local PI3K signaling at cilia in maintaining TZ function.

but levels remain increased compared with wild type, consistent with other studies (Garcia-Gonzalo et al., 2015). No known Hh pathway agonists directly regulate GPR161 signaling. However, active SMO at cilia is essential for the removal of GPR161 from cilia after SAG stimulation by promoting GPR161 binding to β-arrestin and thereby GPR161 endocytosis (Pal et al., 2016). Therefore, the regulation of GPR161 by INPP5E may be integrated and downstream of the INPP5E–SMO signaling axis identified here, allowing for the fine-tuning of Hh signaling.

In summary, we identify INPP5E regulation of PI(4,5)P_2/PI(3,4,5)P_3 at the TZ as a novel mechanism that contributes to TZ function. INPP5E regulation of SMO accumulation at cilia is essential for normal Hh signaling and therefore embryonic development. Collectively, our studies reveal a cooperative signaling network among INPP5E, PIs, and Hh signaling at the TZ.

Materials and methods

Antibodies, constructs, and reagents

Antibodies and organelle stains used were ac-tubulin (Sigma-Aldrich), ARL13B (Neuromab), B9D1 (Novus Biologicals), DAPI (Sigma-Aldrich), FLAG (Sigma-Aldrich), GAPDH (Ambion), GLI1 (Santa Cruz Biotechnology, Inc.), GLI2 (Santa Cruz Biotechnology, Inc.), GPR161 (Proteintech), HA (Covance), HA (Roche), Islet1 (Developmental Studies Hybridoma Bank [DSHB]), Map2 (Cell Signaling Technology), MKS1 (Proteintech), Nkx2.2 (DSHB), Pax6 (DSHB), Pericentrin (Covance), polycystin 2 (Santa Cruz Biotechnology, Inc.), PI(4,5)P_2 (Echelon), PI(3,4,5)P_3 (Echelon), SEPT2 (Sigma-Aldrich), Shh (DSHB), SMO (R. Rohatgi, Stanford University, Stanford, CA; Rohatgi et al., 2007), SMO (Lifespan Biosciences), TCTN1 (Proteintech), TMEM231 (Novus Biologicals), and γ-tubulin (Thermo Fisher Scientific). Alexa Fluor– or HRP-conjugated secondary antibodies were from Thermo Fisher Scientific and GE Healthcare, respectively. All other reagents were from Sigma-Aldrich unless otherwise specified. The Islet1, Nkx2.2, Pax6, and Shh monoclonal antibodies developed by T.M. Jessell and S. Brenner-Morton (Columbia University, New York, NY) were obtained from the DSHB developed under the auspices of the National Institute of Child Health and Human Development and maintained by the Department of Biology at The University of Iowa (Iowa City, IA). pCGN (vector), pCGN-INPP5E (HA-INPP5E), and pCGN-INPP5E(D480N; HA-INPP5E^{D480N}) were described previously (Kong et al., 2000, 2006). V5-INPP5E was described previously (Plotnikova et al., 2015). GFP-PH(Btk) and GFP(PLC) were gifts from T. Balla (National Institutes of Health, Bethesda, MD). HTR6-Tango was a gift from B. Roth (University of North Carolina, Chapel Hill, NC; plasmid 66414; Addgene; Kroeze et al., 2015), mEmerald-MKS1-N-18 was a gift from M. Davidson (Florida State University, Tallahassee, FL; plasmid 54183; Addgene), pCS2+ YFP-SMO was a gift from R. Rohatgi (plasmid 41086; Addgene; Dorn et al., 2012). CEACAM-1-GFP was purchased from OriGene.

Mouse strains

All animal work conformed to ethical standards for animal handling and was approved by MARP2 Monash University animal ethics committee. A targeting construct was generated with *loxP* sites inserted between exons 1 and 2 and exons 6 and 7 and a *FRT* site–flanked neomycin cassette inserted between exons 6 and 7 of the mouse *Inpp5e* gene. Homologous recombination using the targeted *Inpp5e* construct was performed in embryonic stem cells and neomycin-resistant clones selected. Recombinant clones were used to generate C57BL/6 chimeric mice. Progeny of the chimeric mice containing the targeted *Inpp5e* allele were crossed with *Flp* recombinase transgenic mice to generate *Inpp5e*$^{fl/+}$*;flp* mice (Hakim et al., 2016). *Inpp5e*$^{fl/+}$*;flp* mice were backcrossed with *Inpp5e*$^{+/+}$ C57BL/6 mice to remove the recombinase. *Inpp5e*$^{fl/+}$ mice were then crossed with *CMVCre* transgenic mice to generate *Inpp5e*$^{+/-}$*;CMVCre* mice, which were then backcrossed with *Inpp5e*$^{+/+}$ C57BL/6 mice to remove the *CMVCre* transgene. Heterozygous *Inpp5e*$^{+/-}$ matings were used to generate *Inpp5e*$^{-/-}$ embryos.

Gt(ROSA)26Sor$^{tm1(SMO/EYFP)Amc}$*/J* (*SmoM2*) C57BL/6 mice, which have been described previously (Mao et al., 2006), were obtained from N. Watkins (Monash Institute of Medical Research, Melbourne,

Australia). To generate *Inpp5e*$^{-/-}$*;CMVCre;SmoM2*$^{fl/+}$ mice, *Inpp5e*$^{fl/fl}$ mice were crossed with mice expressing constitutively active *SmoM2* to generate *Inpp5e*$^{fl/+}$*;SmoM2* mice. *Inpp5e*$^{fl/fl}$ mice were then crossed with mice expressing *CMVCre* recombinase to generate *Inpp5e*$^{fl/+}$*;CMVCre* mice that were then crossed with *Inpp5e*$^{fl/+}$*;SmoM2* mice to generate *Inpp5e*$^{-/-}$*;CMVCre;SmoM2* mice.

Cell culture and transient transfections

hTERT-RPE1 (RPE) cells were cultured in DMEM-F12 with 10% FCS and 0.01 mg/ml hygromycin and were transfected using Lipofectamine 2000 as per the manufacturer's instructions. For isolation of pMEFs, E12.5 embryos were decapitated and eviscerated and the embryonic tissue minced and incubated in 0.25% trypsin-EDTA using a standard protocol. pMEFs were transfected via nucleofection using the Lonza MEF2 kit with a transfection efficiency of ∼80%.

Immunofluorescence and image analysis

For microscopy, RPE cells or pMEFs were grown on coverslips and serum starved for 24 or 48 h, respectively, to induce cilia and, where indicated, treated with 100 nM SAG for 12–24 h. For PI3K inhibition and PI(3,4,5)P_3 antibody validation, cells were treated with 10 µM LY294003 at 37°C for 1 h before fixation. For PI(4,5)P_2 antibody validation, cells were treated after fixation with 10 mM neomycin for 30 min. For detection of PI(4,5)P_2 at cilia, the "Golgi" staining protocol was used as described previously (Hammond et al., 2009). For detection of PI(3,4,5)P_3 and TZ markers at cilia, cells were fixed with 4% formaldehyde for 20 min, washed three times with PBS, incubated at −20°C in ice-cold methanol for 5 min, and washed three times in PBS. For blocking and antibody dilution 2% BSA in PBS was used. Mouse monoclonal PI(3,4,5)P_3 IgG (Z-P345B; Echelon) was diluted 1:100 and PI(4,5)P_2 IgM (Z-P045; Echelon) diluted 1:1,000. Detection of SMO (Rohatgi et al., 2007), GPR161 (Yee et al., 2015), and GLI2 (Ocbina et al., 2011) was as described previously. Coverslips were mounted onto glass slides with Slowfade Gold (Thermo Fisher Scientific).

Images of Pax6 staining were acquired by confocal microscopy in 10-µm sections taken at the level of the mid–forelimb bud. The surface areas of the total and Pax6-expressing neural tube were outlined using Fiji and expressed as a relative amounts. Four embryos of each genotype (*Inpp5e*$^{+/+}$ and *Inpp5e*$^{-/-}$) were imaged. In the same sections, the position of the ventral and dorsal boundaries of Pax6-expressing cells was expressed relative to total height of the neural tube. The surface area of Pax6-expressing cells as a proportion of the total neural tube was increased in *Inpp5e*$^{-/-}$ embryos ($P = 0.001$). The ventral boundary of Pax6 expression was unchanged relative to the base of the neural tube ($P = 0.42$), but the dorsal boundary was heightened ($P = 0.0003$).

Confocal microscopy was undertaken using either the Nikon C1 Upright confocal setup on the base of an Eclipse 90i microscope with three-channel fluorescence imaging plus transmitted light and four excitation lasers (405 nm, 488 nm, 561 nm, and 635 nm). Single-plane images were captured using the Plan Apo VC 100×/1.40 NA Oil OFN25 DIC N2 WD 0.13 lens and NIS Elements AR (version 4.13) software. Alternatively, confocal microscopy was performed using the Leica Biosystems SP8 Confocal Invert, based on a DMi8 CEL, compact laser unit (405 nm, 488 nm, 550 nm, and 633 nm), XYZ motorized stage, and HyD detector. Single-plane images were captured using the 63× HC PLAPO CS2/1.4 NA Oil WD 0.14 (part 11506350) lens and Leica Biosystems LAS X (version 2.0.1.14392) software.

FRAP

FRAP was performed using a modified method described previously (Fulcher et al., 2010), whereby bleaching of cilia fluorescence and monitoring of the return of fluorescence to the cilia was performed. *Inpp5e*$^{+/+}$ and *Inpp5e*$^{-/-}$ pMEFs transiently expressing YFP-SMO were visualized with a FV1000 CLSM using a100× oil-immersion lens UPlanSApo 100× oil 1.4NA UIS2 (Olympus) and FV10-ASW (version 4.1) software (Olympus). Three images were collected using 1% total laser power with excitation at 488 nm (6× zoom) before photobleaching. For photobleaching, a region of interest (ROI) encompassing ∼90% of the cilium was selected and the 488-nm laser power increased to 50% total laser power and the tornado tool used at a scan speed of 10 µs per pixel for 15 ms. After bleaching, the cells were immediately scanned and the recovery of fluorescence monitored by acquiring subsequent images at 5-s intervals for 6 min using detector and laser settings identical to those used before photobleaching. Image analysis was performed using Fiji (ImageJ public domain software; National Institutes of Health), where Fcilia/c was determined over time. Data were expressed as fractional recovery of Fcilia/c, where each postbleach time point was divided by the mean prebleach Fcilia/c value. The data were then normalized by dividing each time point by the first time point after bleaching (T_0) value, and the fractional recovery and recovery rate ($t_{1/2}$) was determined by exponential curve fitting using GraphPad Software Prism one-phase association curve fitting formulae.

Histology, immunohistochemistry, and in situ hybridization

Alizarin red and alcian blue staining of cartilage and bone, respectively, was performed as described previously (Hogan et al., 1994). Mouse embryonic neural tube samples were frozen and 10-µm sections processed via standard protocols. To examine neural tube and perineural cilia, E10.5 mouse embryos were embedded in paraffin and 8-µm section processed by standard immunohistochemical procedures. For whole-mount in situ hybridization, limb buds were hybridized with riboprobes for *Ptch1*, *GLI1*, and *HoxD13* as previously described (Fowles et al., 2003).

Quantitative RT-PCR

To quantify *Ptch1* mRNA levels in pMEFs, RNA was extracted using the RNeasy mini kit (QIAGEN) and cDNA synthesis performed using the AffinityScript QPCR cDNA Synthesis kit (Agilent Technologies) according to the manufacturer's instructions. Quantitative RT-PCR was performed on the 7900H Fast Real-Time PCR system (Applied Biosystems) using TaqMan 2× PCR MasterMix and *Ptch1* and *Actb* TaqMan probes (Applied Biosystems). Each sample was analyzed in triplicate and normalized to *Actb* expression.

To quantify *Gli1* mRNA levels in pMEFs and *Ptch1* levels in E10.5 embryos, RNA was isolated using the Isolate RNA mini kit (Bioline) and cDNA synthesis performed using the AffinityScript QPCR cDNA Synthesis kit (Agilent Technologies) according to manufacturer's instructions. Quantitative RT-PCR was performed on a Rotor-Gene 3000-qRT-PCR machine using Brilliant II SYBR Green qPCR Master Mix (Agilent Technologies) and *GLI1*, *Ptch1*, and *Gapdh* primers (QIAGEN). Each sample was analyzed in triplicate and normalized to *Gapdh* expression.

Image processing and analysis

Image analysis and processing were performed using FIJI software. To determine the MFI and area of a "candidate" at the TZ, an ROI outlining the ac-tubulin axoneme was transposed onto the candidate channel. The signal proximal to the base of the axoneme was selected and the "mean gray value" and "area" measured and expressed as arbitrary units. To determine the GLI2 MFI specifically at the cilium tip, the ROI encompassing the ac-tubulin axoneme was transposed onto the GLI2 channel. The GLI2 signal detected distal to the ac-tubulin signal (representing the extreme cilium tip) was selected as the ROI and the mean grey value measured and expressed as arbitrary units. To determine the candidate/ac-tubulin ratio, the MFI in the ROI was measured

for the candidate and the corresponding ac-tubulin signal and the ratio calculated and expressed as arbitrary units.

Statistical analysis

Statistical analysis was performed on data from independent experiments. Graphs were generated using GraphPad Software Prism6 and represent mean ± SEM. Statistical significance was evaluated using unpaired two-tailed Student's *t* test and confirmed using the Mann–Whitney μ test for all experiments, with the exception of mice genotype frequency analysis. A χ^2 test was used to compare the observed genotypic frequency versus Mendelian ratios (Fig. 2 mouse studies and Table S1). Differences were considered significant when $P < 0.05$.

Online supplemental material

Fig. S1 shows the phenotype of *Inpp5e*$^{-/-}$ embryos, including developmental abnormalities, aberrant Hh-dependent tissue patterning, reduced Hh signaling, and normal cilia number. Fig. S2 shows the partial rescue of *Inpp5e*$^{-/-}$ phenotypes via expression of constitutively active SMOM2. Fig. S3 shows the cilia localization of wild-type HA-INPP5E and 5-phosphatase–dead HA-INPP5E^{D480N}, as well the reduced cilia accumulation of FLAG-HTR6 and the cilia exclusion of GFP–CEACAM-1 in Hh-stimulated *Inpp5e*$^{-/-}$ pMEFs. Fig. S4 shows $PI(4,5)P_2$ and $PI(3,4,5)P_3$ localize to the cilia TZ and that $PI(4,5)P_2$ and $PI(3,4,5)P_3$ are regulated at cilia by Hh signaling and INPP5E. Fig. S5 shows the colocalization of endogenous TZ markers with a recombinant TZ protein (Emerald-MKS1) to confirm antibody specificity. In addition, the mislocalization of SEPT2 in Hh-stimulated *Inpp5e*$^{-/-}$ pMEFs is shown. Table S1 lists the penetrance of phenotypes in E15.5 *Inpp5e*$^{-/-}$*;CMVCre*, *Inpp5e*$^{+/+}$*;CMVCre;SmoM2* and *Inpp5e*$^{-/-}$*;CMVCre;SmoM2* embryos.

Acknowledgments

We thank Dr. Neil Watkins for the *Gt(ROSA)26Sor*$^{tm1(SMO/EYFP)Amc}$*/J* (*SMOM2*) mice and Dr. Nadia Rosenthal (Australian Regenerative Medicine Institute, Monash University) for assistance with generating *Inpp5e* floxed mice. We thank Rajat Rohatgi for providing the SMO antibody and Gerry Hammond (National Institutes of Health) for technical advice. We acknowledge Monash Micro Imaging (Monash University) and Developmental Studies Hybridoma Bank.

We thank the National Health and Medical Research Council of Australia (APP1046174) for funding. C. Wicking was supported by National Health and Medical Research Council and University of Queensland Vice Chancellor's Senior Research Fellowships, I. Smyth by an Australian Research Council Future Fellow, S.E. Conduit by an Australian Postgraduate award, and S. Hakim by Cancer Council Victoria Postgraduate Cancer Research Scholarship.

The authors declare no competing financial interests.

Submitted: 15 November 2015
Revised: 19 September 2016
Accepted: 2 December 2016

References

Ali-Seyed, M., N. Laycock, S. Karanam, W. Xiao, E.T. Blair, and C.S. Moreno. 2006. Cross-platform expression profiling demonstrates that SV40 small tumor antigen activates Notch, Hedgehog, and Wnt signaling in human cells. *BMC Cancer.* 6:54. http://dx.doi.org/10.1186/1471-2407-6-54

Arts, H.H., D. Doherty, S.E. van Beersum, M.A. Parisi, S.J. Letteboer, N.T. Gorden, T.A. Peters, T. Märker, K. Voesenek, A. Kartono, et al. 2007. Mutations in the gene encoding the basal body protein RPGRIP1L, a nephrocystin-4 interactor, cause Joubert syndrome. *Nat. Genet.* 39:882–888. http://dx.doi.org/10.1038/ng2069

Badrane, H., M.H. Nguyen, J.R. Blankenship, S. Cheng, B. Hao, A.P. Mitchell, and C.J. Clancy. 2012. Rapid redistribution of phosphatidylinositol-(4,5)-bisphosphate and septins during the *Candida albicans* response to caspofungin. *Antimicrob. Agents Chemother.* 56:4614–4624. http://dx.doi.org/10.1128/AAC.00112-12

Badrane, H., M.H. Nguyen, and C.J. Clancy. 2016. Highly dynamic and specific phosphatidylinositol 4,5-bisphosphate, septin, and cell wall integrity pathway responses correlate with caspofungin activity against *Candida albicans*. *Antimicrob. Agents Chemother.* 60:3591–3600. http://dx.doi.org/10.1128/AAC.02711-15

Bae, Y.K., E. Kim, S.W. L'hernault, and M.M. Barr. 2009. The CIL-1 PI 5-phosphatase localizes TRP Polycystins to cilia and activates sperm in *C. elegans*. *Curr. Biol.* 19:1599–1607. http://dx.doi.org/10.1016/j.cub.2009.08.045

Bakrania, P., S.A. Ugur Iseri, A.W. Wyatt, D.J. Bunyan, W.W. Lam, A. Salt, J. Ramsay, D.O. Robinson, and N.K. Ragge. 2010. Sonic hedgehog mutations are an uncommon cause of developmental eye anomalies. *Am. J. Med. Genet. A.* 152A:1310–1313. http://dx.doi.org/10.1002/ajmg.a.33239

Balla, T. 2013. Phosphoinositides: tiny lipids with giant impact on cell regulation. *Physiol. Rev.* 93:1019–1137. http://dx.doi.org/10.1152/physrev.00028.2012

Bielas, S.L., J.L. Silhavy, F. Brancati, M.V. Kisseleva, L. Al-Gazali, L. Sztriha, R.A. Bayoumi, M.S. Zaki, A. Abdel-Aleem, R.O. Rosti, et al. 2009. Mutations in INPP5E, encoding inositol polyphosphate-5-phosphatase E, link phosphatidyl inositol signaling to the ciliopathies. *Nat. Genet.* 41:1032–1036. http://dx.doi.org/10.1038/ng.423

Bridges, A.A., H. Zhang, S.B. Mehta, P. Occhipinti, T. Tani, and A.S. Gladfelter. 2014. Septin assemblies form by diffusion-driven annealing on membranes. *Proc. Natl. Acad. Sci. USA.* 111:2146–2151. http://dx.doi.org/10.1073/pnas.1314138111

Carlton, J.G., and P.J. Cullen. 2005. Coincidence detection in phosphoinositide signaling. *Trends Cell Biol.* 15:540–547. http://dx.doi.org/10.1016/j.tcb.2005.08.005

Casamayor, A., and M. Snyder. 2003. Molecular dissection of a yeast septin: distinct domains are required for septin interaction, localization, and function. *Mol. Cell. Biol.* 23:2762–2777. http://dx.doi.org/10.1128/MCB.23.8.2762-2777.2003

Caspary, T., C.E. Larkins, and K.V. Anderson. 2007. The graded response to Sonic Hedgehog depends on cilia architecture. *Dev. Cell.* 12:767–778. http://dx.doi.org/10.1016/j.devcel.2007.03.004

Cevik, S., A.A. Sanders, E. Van Wijk, K. Boldt, L. Clarke, J. van Reeuwijk, Y. Hori, N. Horn, L. Hetterschijt, A. Wdowicz, et al. 2013. Active transport and diffusion barriers restrict Joubert Syndrome-associated ARL13B/ARL-13 to an Inv-like ciliary membrane subdomain. *PLoS Genet.* 9:e1003977. http://dx.doi.org/10.1371/journal.pgen.1003977

Chávez, M., S. Ena, J. Van Sande, A. de Kerchove d'Exaerde, S. Schurmans, and S.N. Schiffmann. 2015. Modulation of Ciliary Phosphoinositide content regulates trafficking and sonic hedgehog signaling output. *Dev. Cell.* 34:338–350. http://dx.doi.org/10.1016/j.devcel.2015.06.016

Chen, J.K., J. Taipale, K.E. Young, T. Maiti, and P.A. Beachy. 2002. Small molecule modulation of Smoothened activity. *Proc. Natl. Acad. Sci. USA.* 99:14071–14076. http://dx.doi.org/10.1073/pnas.182542899

Chen, M.H., C.W. Wilson, Y.J. Li, K.K. Law, C.S. Lu, R. Gacayan, X. Zhang, C.C. Hui, and P.T. Chuang. 2009. Cilium-independent regulation of Gli protein function by Sufu in Hedgehog signaling is evolutionarily conserved. *Genes Dev.* 23:1910–1928. http://dx.doi.org/10.1101/gad.1794109

Chih, B., P. Liu, Y. Chinn, C. Chalouni, L.G. Komuves, P.E. Hass, W. Sandoval, and A.S. Peterson. 2011. A ciliopathy complex at the transition zone protects the cilia as a privileged membrane domain. *Nat. Cell Biol.* 14:61–72. http://dx.doi.org/10.1038/ncb2410

Corbit, K.C., P. Aanstad, V. Singla, A.R. Norman, D.Y. Stainier, and J.F. Reiter. 2005. Vertebrate Smoothened functions at the primary cilium. *Nature.* 437:1018–1021. http://dx.doi.org/10.1038/nature04117

Delous, M., L. Baala, R. Salomon, C. Laclef, J. Vierkotten, K. Tory, C. Golzio, T. Lacoste, L. Besse, C. Ozilou, et al. 2007. The ciliary gene RPGRIP1L is mutated in cerebello-oculo-renal syndrome (Joubert syndrome type B) and Meckel syndrome. *Nat. Genet.* 39:875–881. http://dx.doi.org/10.1038/ng2039

Ding, Q., J. Motoyama, S. Gasca, R. Mo, H. Sasaki, J. Rossant, and C.C. Hui. 1998. Diminished Sonic hedgehog signaling and lack of floor plate differentiation in Gli2 mutant mice. *Development.* 125:2533–2543.

Dorn, K.V., C.E. Hughes, and R. Rohatgi. 2012. A Smoothened-Evc2 complex transduces the Hedgehog signal at primary cilia. *Dev. Cell.* 23:823–835. http://dx.doi.org/10.1016/j.devcel.2012.07.004

Fowles, L.F., J.S. Bennetts, J.L. Berkman, E. Williams, P. Koopman, R.D. Teasdale, and C. Wicking. 2003. Genomic screen for genes involved in mammalian craniofacial development. *Genesis.* 35:73–87. http://dx.doi.org/10.1002/gene.10165

Francis, S.S., J. Sfakianos, B. Lo, and I. Mellman. 2011. A hierarchy of signals regulates entry of membrane proteins into the ciliary membrane domain in epithelial cells. *J. Cell Biol.* 193:219–233. http://dx.doi.org/10.1083/jcb.201009001

Franco, I., F. Gulluni, C.C. Campa, C. Costa, J.P. Margaria, E. Ciraolo, M. Martini, D. Monteyne, E. De Luca, G. Germena, et al. 2014. PI3K class II α controls spatially restricted endosomal PtdIns3P and Rab11 activation to promote primary cilium function. *Dev. Cell.* 28:647–658. http://dx.doi.org/10.1016/j.devcel.2014.01.022

Fulcher, A.J., M.M. Dias, and D.A. Jans. 2010. Binding of p110 retinoblastoma protein inhibits nuclear import of simian virus SV40 large tumor antigen. *J. Biol. Chem.* 285:17744–17753. http://dx.doi.org/10.1074/jbc.M109.055491

Garcia-Gonzalo, F.R., K.C. Corbit, M.S. Sirerol-Piquer, G. Ramaswami, E.A. Otto, T.R. Noriega, A.D. Seol, J.F. Robinson, C.L. Bennett, D.J. Josifova, et al. 2011. A transition zone complex regulates mammalian ciliogenesis and ciliary membrane composition. *Nat. Genet.* 43:776–784. http://dx.doi.org/10.1038/ng.891

Garcia-Gonzalo, F.R., S.C. Phua, E.C. Roberson, G. Garcia III, M. Abedin, S. Schurmans, T. Inoue, and J.F. Reiter. 2015. Phosphoinositides regulate ciliary protein trafficking to modulate hedgehog signaling. *Dev. Cell.* 34:400–409. http://dx.doi.org/10.1016/j.devcel.2015.08.001

Ghossoub, R., Q. Hu, M. Failler, M.C. Rouyez, B. Spitzbarth, S. Mostowy, U. Wolfrum, S. Saunier, P. Cossart, W. Jamesnelson, and A. Benmerah. 2013. Septins 2, 7 and 9 and MAP4 colocalize along the axoneme in the primary cilium and control ciliary length. *J. Cell Sci.* 126:2583–2594. http://dx.doi.org/10.1242/jcs.111377

Goetz, S.C., and K.V. Anderson. 2010. The primary cilium: a signalling centre during vertebrate development. *Nat. Rev. Genet.* 11:331–344. http://dx.doi.org/10.1038/nrg2774

Hakim, S., J.M. Dyson, S.J. Feeney, E.M. Davies, A. Sriratana, M.N. Koenig, O.V. Plotnikova, I.M. Smyth, S.D. Ricardo, R.M. Hobbs, and C.A. Mitchell. 2016. Inpp5e suppresses polycystic kidney disease via inhibition of PI3K/Akt-dependent mTORC1 signaling. *Hum. Mol. Genet.* 25:2295–2313. http://dx.doi.org/10.1093/hmg/ddw097

Hammond, G.R., S.K. Dove, A. Nicol, J.A. Pinxteren, D. Zicha, and G. Schiavo. 2006. Elimination of plasma membrane phosphatidylinositol (4,5)-bisphosphate is required for exocytosis from mast cells. *J. Cell Sci.* 119:2084–2094. http://dx.doi.org/10.1242/jcs.02912

Hammond, G.R., G. Schiavo, and R.F. Irvine. 2009. Immunocytochemical techniques reveal multiple, distinct cellular pools of PtdIns4P and PtdIns(4,5)P(2). *Biochem. J.* 422:23–35. http://dx.doi.org/10.1042/BJ20090428

Haycraft, C.J., B. Banizs, Y. Aydin-Son, Q. Zhang, E.J. Michaud, and B.K. Yoder. 2005. Gli2 and Gli3 localize to cilia and require the intraflagellar transport protein polaris for processing and function. *PLoS Genet.* 1:e53. http://dx.doi.org/10.1371/journal.pgen.0010053

Heo, W.D., T. Inoue, W.S. Park, M.L. Kim, B.O. Park, T.J. Wandless, and T. Meyer. 2006. PI(3,4,5)P3 and PI(4,5)P2 lipids target proteins with polybasic clusters to the plasma membrane. *Science.* 314:1458–1461. http://dx.doi.org/10.1126/science.1134389

Hogan, B., R. Beddington, F. Costantini, and E. Lacy. 1994. Manipulating the Mouse Embryo: A Laboratory Manual. Cold Spring Harbor Laboratory Press, New York.

Hu, Q., L. Milenkovic, H. Jin, M.P. Scott, M.V. Nachury, E.T. Spiliotis, and W.J. Nelson. 2010. A septin diffusion barrier at the base of the primary cilium maintains ciliary membrane protein distribution. *Science.* 329:436–439. http://dx.doi.org/10.1126/science.1191054

Huang, L., K. Szymanska, V.L. Jensen, A.R. Janecke, A.M. Innes, E.E. Davis, P. Frosk, C. Li, J.R. Willer, B.N. Chodirker, et al. 2011. TMEM237 is mutated in individuals with a Joubert syndrome related disorder and expands the role of the TMEM family at the ciliary transition zone. *Am. J. Hum. Genet.* 89:713–730. http://dx.doi.org/10.1016/j.ajhg.2011.11.005

Hui, C.C., and S. Angers. 2011. Gli proteins in development and disease. *Annu. Rev. Cell Dev. Biol.* 27:513–537. http://dx.doi.org/10.1146/annurev-cellbio-092910-154048

Humbert, M.C., K. Weihbrecht, C.C. Searby, Y. Li, R.M. Pope, V.C. Sheffield, and S. Seo. 2012. ARL13B, PDE6D, and CEP164 form a functional network for INPP5E ciliary targeting. *Proc. Natl. Acad. Sci. USA.* 109:19691–19696. http://dx.doi.org/10.1073/pnas.1210916109

Jacoby, M., J.J. Cox, S. Gayral, D.J. Hampshire, M. Ayub, M. Blockmans, E. Pernot, M.V. Kisseleva, P. Compère, S.N. Schiffmann, et al. 2009. INPP5E mutations cause primary cilium signaling defects, ciliary instability and ciliopathies in human and mouse. *Nat. Genet.* 41:1027–1031. http://dx.doi.org/10.1038/ng.427

Jensen, V.L., C. Li, R.V. Bowie, L. Clarke, S. Mohan, O.E. Blacque, and M.R. Leroux. 2015. Formation of the transition zone by Mks5/Rpgrip1L establishes a ciliary zone of exclusion (CIZE) that compartmentalises ciliary signalling proteins and controls PIP2 ciliary abundance. *EMBO J.* 34:2537–2556. http://dx.doi.org/10.15252/embj.201488044

Jung, B., A.C. Messias, K. Schorpp, A. Geerlof, G. Schneider, D. Saur, K. Hadian, M. Sattler, E.E. Wanker, S. Hasenöder, and H. Lickert. 2016. Novel small molecules targeting ciliary transport of Smoothened and oncogenic Hedgehog pathway activation. *Sci. Rep.* 6:22540. http://dx.doi.org/10.1038/srep22540

Kim, J., M. Kato, and P.A. Beachy. 2009. Gli2 trafficking links Hedgehog-dependent activation of Smoothened in the primary cilium to transcriptional activation in the nucleus. *Proc. Natl. Acad. Sci. USA.* 106:21666–21671. http://dx.doi.org/10.1073/pnas.0912180106

Kisseleva, M.V., M.P. Wilson, and P.W. Majerus. 2000. The isolation and characterization of a cDNA encoding phospholipid-specific inositol polyphosphate 5-phosphatase. *J. Biol. Chem.* 275:20110–20116. http://dx.doi.org/10.1074/jbc.M910119199

Kisseleva, M.V., L. Cao, and P.W. Majerus. 2002. Phosphoinositide-specific inositol polyphosphate 5-phosphatase IV inhibits Akt/protein kinase B phosphorylation and leads to apoptotic cell death. *J. Biol. Chem.* 277:6266–6272. http://dx.doi.org/10.1074/jbc.M105969200

Kong, A.M., C.J. Speed, C.J. O'Malley, M.J. Layton, T. Meehan, K.L. Loveland, S. Cheema, L.M. Ooms, and C.A. Mitchell. 2000. Cloning and characterization of a 72-kDa inositol-polyphosphate 5-phosphatase localized to the Golgi network. *J. Biol. Chem.* 275:24052–24064. http://dx.doi.org/10.1074/jbc.M000874200

Kong, A.M., K.A. Horan, A. Sriratana, C.G. Bailey, L.J. Collyer, H.H. Nandurkar, A. Shisheva, M.J. Layton, J.E. Rasko, T. Rowe, and C.A. Mitchell. 2006. Phosphatidylinositol 3-phosphate [PtdIns3P] is generated at the plasma membrane by an inositol polyphosphate 5-phosphatase: endogenous PtdIns3P can promote GLUT4 translocation to the plasma membrane. *Mol. Cell. Biol.* 26:6065–6081. http://dx.doi.org/10.1128/MCB.00203-06

Kroeze, W.K., M.F. Sassano, X.P. Huang, K. Lansu, J.D. McCorvy, P.M. Giguère, N. Sciaky, and B.L. Roth. 2015. PRESTO-Tango as an open-source resource for interrogation of the druggable human GPCRome. *Nat. Struct. Mol. Biol.* 22:362–369. http://dx.doi.org/10.1038/nsmb.3014

Lambacher, N.J., A.L. Bruel, T.J. van Dam, K. Szymańska, G.G. Slaats, S. Kuhns, G.J. McManus, J.E. Kennedy, K. Gaff, K.M. Wu, et al. 2016. TMEM107 recruits ciliopathy proteins to subdomains of the ciliary transition zone and causes Joubert syndrome. *Nat. Cell Biol.* 18:122–131. http://dx.doi.org/10.1038/ncb3273

Lemmon, M.A. 2008. Membrane recognition by phospholipid-binding domains. *Nat. Rev. Mol. Cell Biol.* 9:99–111. http://dx.doi.org/10.1038/nrm2328

Liscovitch, M., V. Chalifa, M. Danin, and Y. Eli. 1991. Inhibition of neural phospholipase D activity by aminoglycoside antibiotics. *Biochem. J.* 279:319–321. http://dx.doi.org/10.1042/bj2790319

Litingtung, Y., and C. Chiang. 2000. Control of Shh activity and signaling in the neural tube. *Dev. Dyn.* 219:143–154. http://dx.doi.org/10.1002/1097-0177(2000)9999:9999<::AID-DVDY1050>3.3.CO;2-H

Maléth, J., S. Choi, S. Muallem, and M. Ahuja. 2014. Translocation between PI(4,5)P2-poor and PI(4,5)P2-rich microdomains during store depletion determines STIM1 conformation and Orai1 gating. *Nat. Commun.* 5:5843. http://dx.doi.org/10.1038/ncomms6843

Mao, J., K.L. Ligon, E.Y. Rakhlin, S.P. Thayer, R.T. Bronson, D. Rowitch, and A.P. McMahon. 2006. A novel somatic mouse model to survey tumorigenic potential applied to the Hedgehog pathway. *Cancer Res.* 66:10171–10178. http://dx.doi.org/10.1158/0008-5472.CAN-06-0657

Matise, M.P., D.J. Epstein, H.L. Park, K.A. Platt, and A.L. Joyner. 1998. Gli2 is required for induction of floor plate and adjacent cells, but not most ventral neurons in the mouse central nervous system. *Development.* 125:2759–2770.

Matteson, P.G., J. Desai, R. Korstanje, G. Lazar, T.E. Borsuk, J. Rollins, S. Kadambi, J. Joseph, T. Rahman, J. Wink, et al. 2008. The orphan G protein-coupled receptor, Gpr161, encodes the vacuolated lens locus and controls neurulation and lens development. *Proc. Natl. Acad. Sci. USA.* 105:2088–2093. http://dx.doi.org/10.1073/pnas.0705657105

Milenkovic, L., M.P. Scott, and R. Rohatgi. 2009. Lateral transport of Smoothened from the plasma membrane to the membrane of the cilium. *J. Cell Biol.* 187:365–374. http://dx.doi.org/10.1083/jcb.200907126

Mostowy, S., and P. Cossart. 2012. Septins: the fourth component of the cytoskeleton. *Nat. Rev. Mol. Cell Biol.* 13:183–194. http://dx.doi.org/10.1038/nrm3284

Mukhopadhyay, S., X. Wen, B. Chih, C.D. Nelson, W.S. Lane, S.J. Scales, and P.K. Jackson. 2010. TULP3 bridges the IFT-A complex and membrane phosphoinositides to promote trafficking of G protein-coupled receptors

into primary cilia. *Genes Dev.* 24:2180–2193. http://dx.doi.org/10.1101/gad.1966210

Mukhopadhyay, S., X. Wen, N. Ratti, A. Loktev, L. Rangell, S.J. Scales, and P.K. Jackson. 2013. The ciliary G-protein-coupled receptor Gpr161 negatively regulates the Sonic hedgehog pathway via cAMP signaling. *Cell.* 152:210–223. http://dx.doi.org/10.1016/j.cell.2012.12.026

Nalefski, E.A., and J.J. Falke. 1996. The C2 domain calcium-binding motif: structural and functional diversity. *Protein Sci.* 5:2375–2390. http://dx.doi.org/10.1002/pro.5560051201

Ocbina, P.J., J.T. Eggenschwiler, I. Moskowitz, and K.V. Anderson. 2011. Complex interactions between genes controlling trafficking in primary cilia. *Nat. Genet.* 43:547–553. http://dx.doi.org/10.1038/ng.832

Pal, K., S.H. Hwang, B. Somatilaka, H. Badgandi, P.K. Jackson, K. DeFea, and S. Mukhopadhyay. 2016. Smoothened determines β-arrestin-mediated removal of the G protein-coupled receptor Gpr161 from the primary cilium. *J. Cell Biol.* 212:861–875. http://dx.doi.org/10.1083/jcb.201506132

Park, J., N. Lee, A. Kavoussi, J.T. Seo, C.H. Kim, and S.J. Moon. 2015. Ciliary phosphoinositide regulates ciliary protein trafficking in *Drosophila*. *Cell Reports.* 13:2808–2816. http://dx.doi.org/10.1016/j.celrep.2015.12.009

Plotnikova, O.V., S. Seo, D.L. Cottle, S. Conduit, S. Hakim, J.M. Dyson, C.A. Mitchell, and I.M. Smyth. 2015. INPP5E interacts with AURKA, linking phosphoinositide signaling to primary cilium stability. *J. Cell Sci.* 128:364–372. http://dx.doi.org/10.1242/jcs.161323

Reiter, J.F., O.E. Blacque, and M.R. Leroux. 2012. The base of the cilium: roles for transition fibres and the transition zone in ciliary formation, maintenance and compartmentalization. *EMBO Rep.* 13:608–618. http://dx.doi.org/10.1038/embor.2012.73

Riobó, N.A., K. Lu, X. Ai, G.M. Haines, and C.P. Emerson Jr. 2006. Phosphoinositide 3-kinase and Akt are essential for Sonic Hedgehog signaling. *Proc. Natl. Acad. Sci. USA.* 103:4505–4510. http://dx.doi.org/10.1073/pnas.0504337103

Roberson, E.C., W.E. Dowdle, A. Ozanturk, F.R. Garcia-Gonzalo, C. Li, J. Halbritter, N. Elkhartoufi, J.D. Porath, H. Cope, A. Ashley-Koch, et al. 2015. TMEM231, mutated in orofaciodigital and Meckel syndromes, organizes the ciliary transition zone. *J. Cell Biol.* 209:129–142. http://dx.doi.org/10.1083/jcb.201411087

Rohatgi, R., L. Milenkovic, and M.P. Scott. 2007. Patched1 regulates hedgehog signaling at the primary cilium. *Science.* 317:372–376. http://dx.doi.org/10.1126/science.1139740

Rohatgi, R., L. Milenkovic, R.B. Corcoran, and M.P. Scott. 2009. Hedgehog signal transduction by Smoothened: pharmacologic evidence for a 2-step activation process. *Proc. Natl. Acad. Sci. USA.* 106:3196–3201. http://dx.doi.org/10.1073/pnas.0813373106

Sang, L., J.J. Miller, K.C. Corbit, R.H. Giles, M.J. Brauer, E.A. Otto, L.M. Baye, X. Wen, S.J. Scales, M. Kwong, et al. 2011. Mapping the NPHP-JBTS-MKS protein network reveals ciliopathy disease genes and pathways. *Cell.* 145:513–528. http://dx.doi.org/10.1016/j.cell.2011.04.019

Slaats, G.G., C.R. Isabella, H.Y. Kroes, J.C. Dempsey, H. Gremmels, G.R. Monroe, I.G. Phelps, K.J. Duran, J. Adkins, S.A. Kumar, et al. 2016. MKS1 regulates ciliary INPP5E levels in Joubert syndrome. *J. Med. Genet.* 53:62–72. http://dx.doi.org/10.1136/jmedgenet-2015-103250

Slavotinek, A.M. 2011. Eye development genes and known syndromes. *Mol. Genet. Metab.* 104:448–456. http://dx.doi.org/10.1016/j.ymgme.2011.09.029

Szymanska, K., and C.A. Johnson. 2012. The transition zone: an essential functional compartment of cilia. *Cilia.* 1:10. http://dx.doi.org/10.1186/2046-2530-1-10

Thomas, S., K.J. Wright, S. Le Corre, A. Micalizzi, M. Romani, A. Abhyankar, J. Saada, I. Perrault, J. Amiel, J. Litzler, et al. 2014. A homozygous PDE6D mutation in Joubert syndrome impairs targeting of farnesylated INPP5E protein to the primary cilium. *Hum. Mutat.* 35:137–146. http://dx.doi.org/10.1002/humu.22470

Travaglini, L., F. Brancati, J. Silhavy, M. Iannicelli, E. Nickerson, N. Elkhartoufi, E. Scott, E. Spencer, S. Gabriel, S. Thomas, et al. International JSRD Study Group. 2013. Phenotypic spectrum and prevalence of INPP5E mutations in Joubert syndrome and related disorders. *Eur. J. Hum. Genet.* 21:1074–1078. http://dx.doi.org/10.1038/ejhg.2012.305

Vieira, O.V., K. Gaus, P. Verkade, J. Fullekrug, W.L. Vaz, and K. Simons. 2006. FAPP2, cilium formation, and compartmentalization of the apical membrane in polarized Madin-Darby canine kidney (MDCK) cells. *Proc. Natl. Acad. Sci. USA.* 103:18556–18561. http://dx.doi.org/10.1073/pnas.0608291103

Wang, Y., Z. Zhou, C.T. Walsh, and A.P. McMahon. 2009. Selective translocation of intracellular Smoothened to the primary cilium in response to Hedgehog pathway modulation. *Proc. Natl. Acad. Sci. USA.* 106:2623–2628. http://dx.doi.org/10.1073/pnas.0812110106

Waters, A.M., and P.L. Beales. 2011. Ciliopathies: an expanding disease spectrum. *Pediatr. Nephrol.* 26:1039–1056. http://dx.doi.org/10.1007/s00467-010-1731-7

Wei, H.C., J. Rollins, L. Fabian, M. Hayes, G. Polevoy, C. Bazinet, and J.A. Brill. 2008. Depletion of plasma membrane PtdIns(4,5)P2 reveals essential roles for phosphoinositides in flagellar biogenesis. *J. Cell Sci.* 121:1076–1084. http://dx.doi.org/10.1242/jcs.024927

Williams, C.L., C. Li, K. Kida, P.N. Inglis, S. Mohan, L. Semenec, N.J. Bialas, R.M. Stupay, N. Chen, O.E. Blacque, et al. 2011. MKS and NPHP modules cooperate to establish basal body/transition zone membrane associations and ciliary gate function during ciliogenesis. *J. Cell Biol.* 192:1023–1041. http://dx.doi.org/10.1083/jcb.201012116

Wong, S.Y., A.D. Seol, P.L. So, A.N. Ermilov, C.K. Bichakjian, E.H. Epstein Jr., A.A. Dlugosz, and J.F. Reiter. 2009. Primary cilia can both mediate and suppress Hedgehog pathway-dependent tumorigenesis. *Nat. Med.* 15:1055–1061. http://dx.doi.org/10.1038/nm.2011

Wu, V.M., S.C. Chen, M.R. Arkin, and J.F. Reiter. 2012. Small molecule inhibitors of Smoothened ciliary localization and ciliogenesis. *Proc. Natl. Acad. Sci. USA.* 109:13644–13649. http://dx.doi.org/10.1073/pnas.1207170109

Xie, J., M. Murone, S.M. Luoh, A. Ryan, Q. Gu, C. Zhang, J.M. Bonifas, C.W. Lam, M. Hynes, A. Goddard, et al. 1998. Activating Smoothened mutations in sporadic basal-cell carcinoma. *Nature.* 391:90–92. http://dx.doi.org/10.1038/34201

Yang, T.T., J. Su, W.J. Wang, B. Craige, G.B. Witman, M.F. Tsou, and J.C. Liao. 2015. Superresolution pattern recognition reveals the architectural map of the ciliary transition zone. *Sci. Rep.* 5:14096. http://dx.doi.org/10.1038/srep14096

Yee, L.E., F.R. Garcia-Gonzalo, R.V. Bowie, C. Li, J.K. Kennedy, K. Ashrafi, O.E. Blacque, M.R. Leroux, and J.F. Reiter. 2015. Conserved genetic interactions between ciliopathy complexes cooperatively support ciliogenesis and ciliary signaling. *PLoS Genet.* 11:e1005627. http://dx.doi.org/10.1371/journal.pgen.1005627

Yip, S.C., R.J. Eddy, A.M. Branch, H. Pang, H. Wu, Y. Yan, B.E. Drees, P.O. Neilsen, J. Condeelis, and J.M. Backer. 2008. Quantification of PtdIns(3,4,5)P(3) dynamics in EGF-stimulated carcinoma cells: a comparison of PH-domain-mediated methods with immunological methods. *Biochem. J.* 411:441–448. http://dx.doi.org/10.1042/BJ20071179